Journal of Superconductivity and Novel Magnetism (2020) 33:629–660
https://doi.org/10.1007/s10948-019-05204-7

ORIGINAL PAPER

The Additive Approximation for Heat Transfer and for Stability Calculations in a Multi-Filamentary Superconductor—Part B

Harald Reiss [1]

Received: 8 March 2019 / Accepted: 1 July 2019 / Published online: 23 August 2019

Abstract
A hypothesis shall be confirmed: Non-convergence of a series of numerical solutions, to simulate transient temperature under increasing losses in a superconductor, might tightly be correlated with the superconducting to normal conducting phase transition. Consider as an analogue a standard, mathematical power series expansion: While the exact limit cannot be captured within the series, there is no doubt about its existence. A series of numerical solutions in stability analysis is considered a parallel to the mathematical series convergence problem: Likewise, there is no doubt that a limit of the numerical solution series exists (the phase transition) but it cannot be reached within the series. The concept is applied to multi-filamentary BSCCO 2223 and coated, thin film YBaCuO 123 superconductors and to NbTi superconductor filaments. Support is provided by a microscopic stability model and from comparison of order parameters. Simulation of current transport near phase transitions may become severely in error if length of load steps is in conflict with time needed for its completion.

Keywords Numerical simulations · Finite element method · Additive approximation · BSCCO · YBaCuO · NbTi · Superconductor stability · Conductor temperature · Convergence · Quench · Phase transition · Order parameter · Quantum states

1 Introduction

1.1 Overall Description of the Quench Problem

Consider a sudden superconducting to normal conducting phase transition when a superconducting filament or tape is subject to a strong disturbance; usually, this is interpreted as a quench, a most undesirable event. A quench can lead to severe damage of the superconductor and possibly to its total destruction, a catastrophic failure. The physics behind quenching is conversion of stored electromagnetic energy, originating from screening and transport currents, to thermal energy, within very short time.

The calculations described in this paper are concentrated on high-temperature superconductors, with numerical simulations of their stability against quench and of phase changes when conductor temperature exceeds critical temperature. The numerical method should in principle be applicable to thermodynamic phase changes in also other solids or thin films, not only to standard ($T > 0$) superconducting to normal conducting phase transitions, when temperature constitutes the degree of freedom.

A physical system can perform phase transitions also at $T = 0$, namely quantum phase transitions, then under other than temperature variations, as degree of freedom (pressure, magnetic field, chemical composition). We will come back to quantum phase transitions in Sects. 2.4 and 5.3, but only under a specific aspect that is interesting for interpretation of the results obtained in the simulations with superconductors.

Assume for the moment that the electromagnetic energy, provided by a current of momentary density, J, is distributed uniformly to the volume of a superconductor, a magnet coil, for example. The simple electrical/thermal energy balance (Wilson [1], p. 201) allows estimating a mean (stagnation) temperature, T_m, from

$$\int_0^\infty \rho_{el}(t) J^2(t) dt = \int_0^{T_m} \rho_{cp}(T) dT \tag{1.1}$$

to which the system temperature converges. In Eq. (1.1), ρ_{el} and ρ denote electrical resistivity and density and c_p the specific heat. The electromagnetic energy shall be distributed

✉ Harald Reiss
harald.reiss@physik.uni-wuerzburg.de

[1] Department of Physics, University of Wuerzburg, Am Hubland, 97074 Wuerzburg, Germany

instantly, not only spatially, after each variation of J or of ρ_{el}, to the total volume. The solution for T_m in this case yields a very small temperature increase against the initial state.

This balance, under the condition that the energy is uniformly distributed, implies that also the conductor temperature, T, in each integration step would be uniform in the conductor volume.

In reality, this is never fulfilled. Quench starts locally, and as soon as conductor temperature exceeds critical temperature, Ohmic heating and thermal conduction quickly contribute to increase the volume of the developing normal zone, which increases the resistance of the conductor (and leads to decay of J). Further, again in reality, the quantities ρ_{el}, J^2, c_p and T in Eq. (1.1) are not constant but can strongly fluctuate, in time and in position, within the conductor.

The magnet current (in nominal operation or possibly from a fault) will finally either almost completely disappear or by means of current limiters be reduced to a tolerable level (or simply be switched off by conventional methods). However, before this level is reached, the conductor could be destroyed.

Quench can be avoided by application of stability models [1–3]. These models favour tight mechanical, electrical and thermal conductive and radiative coupling of the superconductor to its ambient (like its embedding in a metallic matrix or by close contact to a stabilising metallic coating). Standard stability models resemble Eq. (1.1), except that they include a heat sink like a stabilising coating or the cooling system.

Another view of a quench, different from the traditional condition ($T < T_{Crit}$) to avoid quenching, can be taken by considering the density, $n_S(T)$, of electron pairs in equilibrium states of the superconductor. In order to support zero loss of screening and transport currents in the superconductor, a minimum density, $n_{S0}(T)$, is required. In case the available density of electron pairs becomes too small, $n_S(T) < n_{S0}(T)$, zero loss current transport can no longer be provided by the superconductor.

It is thus not only the traditional condition, $T < T_{Crit}$, that should be considered in order to protect the superconductor against quench. A prognosis whether quenching has to be expected or not can be substantiated more securely by comparing $n_S(T)$ with $n_{S0}(T)$. The condition $n_S(T) > n_{S0}(T)$ has to be fulfilled at all temperatures, $T = T(t)$, during a disturbance.

The two conditions, $T < T_{Crit}$ and $n_S(T) > n_{S0}(T)$, not necessarily are equivalent. If $n_S(T) > n_{S0}(T)$, zero loss current transport will be possible. But the strong dependency of $n_S(T)$ on temperature, in particular if T is very close to T_{Crit}, and thermal fluctuations might lead to a situation where the condition $n_S(T) > n_{S0}(T)$ no longer can be fulfilled even if $T < T_{Crit}$. See later, Sect. 6 (Fig. 8a; Table 1).

Background of all standard stability models are energy balances, which like Eq. (1.1) are either reduced to comparison of temperatures ($T < T_{Crit}$) or like Eqs. (7.5) to (7.7) in [1] define a stability parameter, β, which requests

$$\beta = \mu_0 {J_{Crit}}^2 a^2 / [\rho\, C\, (T_{Crit} - T_0)] < 3 \qquad (1.2)$$

to be fulfilled, under adiabatic conditions. In Eq. (1.2), μ_0, J_{Crit}, a, ρ, C, T_{Crit} and T_0 in this order denote electromagnetic constant, critical current density, half thickness of a superconductor slab, material density and specific heat, critical and coolant temperature, respectively (the integer 3 results from integration over slab thickness in the derivation of this equation).

Expressions like Eq. (1.2) for other than flat plate geometry can be found in [1]. The extension of the adiabatic (Eq. 1.1, 2) to dynamic stability, to include heat transfer to a coolant, is reported in Eq. (7.22) of the same reference.

A real, observable temperature increase, ΔT, is not found in Eq. (1.2). It is replaced, after some algebra ([1], p. 134), by the difference $(T_{Crit} - T_0)$, the maximum temperature

Table 1 Calculated density, $n_S(T)$, of electron pairs in YBaCuO 123 at given temperature. Column 2: Values calculated using the microscopic stability model [13], column 3: calculated from Eq. (5a,b), in dependence of critical current density at local temperature

Temperature (K)	Density $n_S(T)$ (1/m^3)	Density $n_{S0}(T)$ (1/m^3)	Difference [$n_S(T)$ - $n_{S0}(T)$] (1/m^3)
90.5	6.665E+25	6.1321E+22	6.659206E+25
91	5.442E+25	4.0881E+22	5.438138E+25
91.25	4.713E+25	3.0661E+22	4.710040E+25
91.5	3.848E+25	2.044E+22	3.846191E+25
91.6	3.442E+25	1.6352E+22	3.440331E+25
91.7	2.981E+25	1.2264E+22	2.979604E+25
91.8	2.434E+25	8.1762E+21	2.433020E+25
91.9	1.721E+25	4.0881E+21	1.720574E+25
91.99	5.442E+24	4.0881E+20	5.441817E+24
91.999	1.721E+24	4.0881E+19	1.720959E+24
91.9999	3.159E+19	4.0881E+18	2.749876E+19
91.99999	*3.159E+15*	*4.0881E+17*	*− 4.056491E+17*

difference that can exist within the slab as long as the slab remains in its superconducting state. In an experiment, an effective specific capacity

$$\rho C_{eff} = \Delta Q/\Delta T = \rho C - \mu_0 J_{Crit}{}^2 a^2/[3\ (T_{Crit} - T_0)] \quad (1.3)$$

would be observed if an amount of heat, ΔQ, is supplied to the sample (e.g. from a disturbance). If $\mu_0\ J_{Crit}{}^2\ a^2/[3\ \rho\ (T_{Crit} - T_0)]$ equals $\rho\ C$, the effective heat capacity $\rho\ C_{eff}$ goes to zero. Even a tiny amount of heat, ΔQ, supplied to the conductor then would be sufficient to drive sample temperature to divergence and to flux jump.

The adiabatic stability criterion thus is given by

$$\rho C - \mu_0 J_{Crit}{}^2 a^2/[3\ (T_{Crit} - T_0)] > 0 \quad (1.4)$$

that can be solved for the slab thickness, $a^2 < [3\ \rho\ C\ (T_{Crit} - T_0)]/(\mu_0\ J_{Crit}{}^2)$.

Equations (1.2) to (1.4) and their extensions consider the energy balance extended over the whole superconductor cross section (or volume), here a slab, which is assumed as homogeneous in all its materials and transport properties. However, under heat sources (disturbances that create losses), with contact of the superconductor to a coolant, and if the sample material consists of components of different thermal diffusivity, its temperature cannot be uniform, neither spatially nor temporally except for vanishing sources and sinks and when time $t \to \infty$. Without modifications, standard adiabatic and dynamic stability models like Eqs. (1.2) to (1.4) become questionable if they are applied to, for example, superconductor filaments embedded in a normal conducting matrix. Safety margins are applied to predictions from these models to make sure the conductor will not quench also in these cases.

This situation can be improved. Instead of checking $T < T_{Crit}$ or $\beta < 3$, control of superconductor stability could be performed, though very challengingly, by considering the difference between the Helmholtz or Ginzburg-Landau free energies of superconducting and normal conducting states (with zero or non-zero magnetic field, respectively), in relation to the energy released by a disturbance. In case of strongly inhomogeneous conductor temperature, application of this method would become too complicated.

As a method more suitable (and by no means less challenging), especially in case of detailed conductor geometry, inhomogeneous material composition and inhomogeneous temperature distribution, we suggest numerical simulations. While such calculations may request enormous computational efforts, they have the advantage that each calculation step can be designed appropriately, step by step with energy balances on a micro-level in small conductor elements (by a finite element method), and they can be controlled comparatively easily by inspection of the obtained results.

The whole spectrum of transient or continuous disturbances in superconductors is large, compare e.g. [1], Chap. 5. Disturbances usually proceed on time-scales of milliseconds and below. While this constitutes a typical, short-time physics problem, quench may become a self-amplifying event, even if numerically modelled in small time steps, above a certain temperature level, under a strong disturbance and if transport current is not limited or switched off.

1.2 A Hypothesis

This paper continues with discussion of a hypothesis that was raised at the end of part A of the paper: Non-convergence of an applied numerical scheme for calculation of transient temperature fields in a superconductor might tightly be correlated with the onset of the superconducting to normal conducting phase transition. See DOI https://doi.org/10.1007/s10948-019-5103-7.

The hypothesis is suggested on the basis of an apparently existing correlation between two spaces:

1. The experimental situation (the "physical reality") of the simulated superconductor and its development with time, under any variation of internal energy states and thermodynamic variables (temperature, magnetic field and current, in particular their critical ones). These shall in the following be addressed as "events".

2. The results of the simulation (the "numerical space") that as an "image", or as a series of images, should reflect the experimental reality (the events) as precisely as possible.

Like in part A of the paper, the correlation "events/images", if it exists, in the ideal case relies on a one-to-one correspondence between both spaces (1) and (2). For all events located in space (1), the experimental space, like temperature, magnetic field or transport current variations and in particular the impacts of a disturbance or of a quench, images of these events should (a) *exist* in the numerical space (2) and (b) unambiguously be *correlated* with events in the physical space (1). For this purpose, the correspondence, if it is interpreted as a kind of mapping, must be bijective between both spaces, which means it must be injective and surjective, in the usual mathematical sense. The correspondence also must exist irrespective of the number of events and images.

Precise predictions of the future of the system, in the present case the approach to the possible occurrence of a quench in a superconductor, the time when it is to be expected and whether or not the whole superconductor volume or only part of it would be concerned, can be made only on the basis of such a correspondence.

But the problem is how to appropriately simulate, by numerical methods, the close approach of the superconductor,

during a disturbance, to its critical states and how to predict time and position of the real occurrence of a quench in the superconductor? Not only must the method avoid uncertainties always inherent in numerical simulations and in the input (the quality) of physical parameters. The correspondence, once identified, also must be *conserved* throughout the progress of the simulation, and it must be shown that it can be supervised and eventually be adapted according to the obtained results.

Numerical procedures in finite element calculations are interrupted when divergence of the results occurs or if divergence can safely be anticipated. The results obtained so far are the "normal" completed, converged solutions. Finite element computer codes indicate the number of completed equilibrium iterations before the series diverges and is terminated (the output signal is arbitrary, like a number "99999" in the list of completed equilibrium iterations). In the finite element calculations, each of the load steps declared in this paper for this reason is divided into presently up to 10 sub-steps a...k that each perform finite element equilibrium iterations until convergence, with the sub-steps a...k of smaller and smaller length in time; compare Fig. 12 in Appendix 1.

The number of problems with the simulation of transient temperature distribution in the conductors obviously is large. But examples found in other disciplines, like in fracture mechanics with successful stability analysis, prediction of irreversible system break-down and how to avoid it, exothermic chemical reactions or nuclear engineering when these systems, again under disturbances, approach critical states, provides motivation to extend these successful investigations to also superconductors.

All results of the calculations in the following have to be understood as those of quasi-equilibrium states of the conductor; they are successively but individually obtained in the series of load steps and sub-steps. Physically, the quasi-equilibrium states, in reality, not within the load steps of the simulations, are *dynamic* equilibrium states since decay of electron pairs and recombination occurs at all temperatures $T > 0$.

1.3 How to Prove the Hypothesis

A rigorous proof of the correlation mentioned in the previous subsection would hardly be possible, but the results of numerical calculations of transient temperature distributions, stability functions and electron pair density in the superconductors shall be interpreted as like elements of a mathematical power series, with a limit to which the series converges. While the exact limit of a mathematical power series cannot be captured *within* the series, no one has doubt about its existence, which usually can be proven by elementary algebra.

A parallel to this mathematical power series is the results obtained in the simulated load steps under continuously increasing losses due to strong disturbances in a multi-filamentary BSCCO 2223, or a coated, thin-film YBaCuO 123 tape, or a NbTi superconductor filaments. There is again no doubt that a limit of also this series exists: It is the superconductor to normal conductor phase transition of which time and position of its occurrence cannot be reached as a converged solution *within* the series. But it is clear the transition, under the given conditions, will occur. The series can be extended, by the number of load steps and sub-steps a...k to as close as numerically possible approach the anticipated quench.

It is this concept that shall be pursued in this paper: By application of appropriate numerical simulation tools, show that a series of *converged* solutions in given load steps exists that approach the *divergent* final state of the superconductor system, as close as numerically possible, though this final state (the phase transition) cannot be reached during the simulations.

In order to be successful, this procedure must avoid all well-known short-cuts of traditional stability models.

First, these models assume worst-case scenarios to obtain conservative solutions of the stability problem. This implies the temperature distribution in the conductor cross section is uniform, at appropriately chosen levels. But recently obtained results from numerical simulations demonstrate that (transient) temperature distributions under disturbances might not at all be uniform (see later, Sect. 5).

There are at least five more weaknesses: The traditional models assume

1. Homogeneous distribution and a quasi-laminar flow (no percolation) of transport current
2. Assume instantaneous distribution and thermalisation of a local or of an extended disturbance
3. Do not precisely specify the particular type, its location, temporal sequence (if any) and intensity of the disturbance
4. Restrict thermal dissipation of a disturbance, and the resulting temperature variations, simply to only conduction heat transfer (while in thin films, radiative transfer, the transparency of the sample, must be included)
5. Describe boiling heat transfer to a coolant frequently with only constant (independent of temperature) heat transfer coefficients which, like the other short-cuts, may cause severe errors

1.4 Details of the Simulations

The numerical stability model that is applied in the present paper (an iteratively operating "master" scheme) tries to avoid the problems of standard stability models, items (1) to (5). In particular, numerical stability calculations (Sect. 5) have predicted, as the consequence of strongly inhomogeneous temperature distributions within the conductor, percolating current flow (compare Appendix 2 in [4] and Fig. 6a,b in [5]).

The applied solution scheme in this paper, to verify the above mentioned hypothesis, is by no means perfect. Though the short-cuts of standard stability models can be avoided, more uncertainties originate from:

1. The finite element procedure itself (the numerical problem) and from the physical models that subsequently apply its solutions (the temperature field as resulting from Fourier's differential equation). We have to concentrate on the most important, potential error sources. In the finite element simulations of superconductor states, these comprise meshing, convergence criteria, the idea that heat transfer can be modelled as a diffusion-like process (with also radiation proceeding by a diffusion-like mechanism), simulations of energy sources and sinks like heat transfer to the coolant.
2. Under the physical, material properties and transport aspects, it is the potential uncertainty arising from magnitude of the resistances, in particular the flux flow resistance (the loss that comes up before the system enters the Ohmic resistance state). Serious uncertainties also may arise from differences seen in many reported, experimental values of critical temperature and current density.

The list of uncertainties potentially arising from finite element steps and from data input is large; they all may question the calculated numerical solutions.

To continue with item (1), a finite element (FE) simulation code has been embedded into the already mentioned, numerical iterative master scheme to calculate, in a series of load steps, the transient temperature field, T(x,y,t). After completion of the FE procedure in each load step (which means after convergence has been achieved in this load step or this sub-step), the master scheme calculates electrical and magnetic states, critical values of T, B and current density, J, and the distribution of transport current in the cross section of the superconductor. The master scheme will be explained in detail in Appendix 1.

Since the procedures are designed as numerical approach to the critical state, and since this state strongly depends on variations of any load that it is subject to, they have to be carried out in time steps the length of which must be short against relaxation times that the physical system needs to proceed from one quasi-equilibrium state (obtained in one load step or sub-step) to the next. The number of load steps thus will become large.

No analytical solution seems to be possible that could provide the same degree of accuracy, irrespective of the potential uncertainties mentioned above. Like in investigations of unstable crack propagation in fracture mechanics, the superconductor, under a strong disturbance, approaches a "point of no return" (as can be expected from part A, Fig. 16, the solid black diamonds) after which it, being in a thermal excitation state, invariably will become unstable: The larger its temperature, the smaller the number of coupled electrons to carry a zero loss current, and thus the smaller its critical current density, which in an application might get into conflict with transport current.

Analysis of superconductor stability based simply on comparison of the thermodynamic variable, T(x,y,t), with its critical value, T_{Crit}(x,y,t), would not be sufficient for unambiguously establishing the said anticipated correlation. Local temperature is the result of temperature-dependent transport processes in the superconductor, and both critical magnetic field, B_{Crit}(x,y,t), and critical current density, J_{Crit}(x,y,t), strongly depend on T(x,y,t) and vice-versa. Excursion with time of local temperature, therefore, is a first key for the following numerical analysis, and it is not a contradiction to the previous statement that considering *solely* temperature would not be sufficient for stability analysis (without considering the relation between requested and available density of electron pairs).

The computer program "QUENCH" (Wilson [1], p. 218) apparently is one of the first numerical tools to calculate quenching. Its modelling of an ellipsoid of increasing normal conductor volume in a superconductor, layer by layer, assumes isothermal conditions in each layer. The tool also accepts anisotropic materials and electrical/thermal transport conditions in the solution process. But assuming isothermal conditions in each layer is not very suitable to application in both multifilamentary and thin film superconductors because of large anisotropy of transport properties.

To proceed with item (2) of the above, experimental thermal diffusivity and radiative contributions (corrections) to conduction heat transfer in this paper have been taken from the literature (the additive approximation of total thermal conductivity has been applied to obtain a total thermal conductivity, a procedure the validity of which has been proven with the same superconductors in part A). Impact of mid-IR radiation contributions to heat transfer in multi-filamentary and in thin film superconductors has been investigated in our previous papers by application of rigorous scattering theory. Though radiative contributions to heat transfer in a bulk solid material are vanishingly small, this is not necessarily the case with thin films.

Statistical variations against mean values of critical superconductor variables (T_{Crit}, J_{Crit}, lower and upper field B_{Crit}) are applied to account for uncertainties arising from incomplete knowledge of their proper, exact values (Fig. 16 in Appendix 3). We will not explicitly include thermal fluctuations near critical temperature; instead, they indirectly shall be taken into account by (small) random variations of T_{Crit} around its mean value, in BSSCO 2223, YBaCuO 123 and NbTi superconductors. These variations are different in each of the numerous, tiny elements in the finite element calculations. Size of the random values is explained in [4].

Simulation of the transport current distribution in this paper is made by means of a conventional (in its geometrical design) Kirchhoff resistance network (with transient values of the single resistances, however): It is assumed the network distributes current instantaneously, on a time scale that numerically is very

small (quasi-zero) against corresponding (electrical, thermal) relaxation constants of the superconductor system. The "quasi-zero" time constant of the *physical* process of current distribution itself thus, fortunately, does not need to be modelled explicitly. Once the individual (transient) resistances of all elements are calculated in each load step, j, current distribution is modelled from one quasi-stationary state (j) to the next ($j + 1$), as an instantaneously completed process (provided convergence in load step, j, has been obtained already).

Compare as an example Fig. 13 in Appendix 1: Convergence temperature is indicated schematically by the large, solid red circles, at the end of each of the loads steps, j. When the system arrives at its convergence temperature, redistribution of transport current and of all electrical variables occurs quasi-instantaneously. Any attempt to specifically model the proper *physica*l process of current redistribution would lead to enormous complications: While both physical systems (electrical vs. thermal transport processes) numerically proceed in parallel, there are large differences between their development with time.

Very close to the phase transition, a problem concerning current redistribution can arise from the length, Δt, of load steps in the numerical simulations in relation to the time constant, τ_{El}, for decay of electron pairs or recombination of single electrons to pairs during heating or cooling or under strong current density variations, respectively. It is not clear that the phase transition will always be completed within this period so that complications might arise that not only concerns current redistribution; see Sect. 6.3.

In [6], we concluded that a filament in a multi-filamentary conductor, and even a superconductor thin film, is non-transparent to mid-IR radiation (if sample thickness is standard, as in usual cases of current transport). This result enormously simplifies the analysis. There are alternatives like the combined Monte Carlo/finite element procedure described in [7] that might be consulted as well. These procedures constitute a more direct approach to radiative transfer, instead of its somehow "blurred" imagination as being simply a diffusion process. But they would introduce more uncertainties and would strongly increase computation time.

Non-transparency of the superconductor, accordingly, is the second key to solve the said correspondence problem (it might allow another problem, definition of a physical time scale, to again come in through the back door, however; see Sect. 6.4).

2 Specification of the Conductors

2.1 First Generation, Multi-Filamentary BSCCO Superconductors

Properties of the "first-generation" (1G) BSCCO 2223 superconductor filaments and tapes prepared in the Powder in Tube manufacturing process have already been described in part A and will not be repeated here (some more details can be found in Appendix 2 to this paper). In short, the tape consists of filaments of superconductor material embedded in a metallic (Ag) matrix to form a thin film. The filaments in turn consist of thin, flat plate-like superconductor grains.

A successful realisation of this Powder in Tube manufacturing concept was achieved with the tape of the BSCCO 2223/Ag Long Island Cable superconductor [8]; compare Figs. 1a-c and 2ab in part A.

Electrical and thermal transport properties of the BSCCO 2223 material are strongly different from the properties of the Ag matrix, and also are highly anisotropic. The same applies to microscopic parameters like field penetration and coherence length. Each filament by surface roughness and weak links (quasi-surface inter-layers) is to some extent electrically and thermally decoupled from its neighbours and from the Ag-matrix material.

Onset of the Meissner effect within each filament may be quite different, because of the same decoupling of the filament from its neighbours. It depends on the local magnetic field and thus on local temperature.

Finally, calculations of heat transfer from this object to a coolant become a challenging task, too.

2.2 Second-Generation, Coated Thin-Film YBaCuO 123 Superconductors

Calculations of transient temperature distribution in the other (presently more attractive) superconductor, the coated, thin film YBaCuO 123 tape applied in a coil, have been described in [9]. The stability analysis in this conductor, as seen from the numerical simulation aspect, is less complicated because the many superconductor/matrix interfaces in the BSCCO system are replaced by plane (2D) interfacial contacts to other thin layers (substrates, coatings), and the anisotropy of electrical and thermal transport is less pronounced.

Details of the conductor are explained in Fig. 1 of [9] and will not be repeated here. Again in short, the overall design of the simulation scheme addresses a coil with 100 turns (only the outermost five windings are simulated). Conductor architecture is standard, but very thin, interfacial, insulating layers exist between superconductor film and Ag (metallization) and between superconductor and MgO (buffer layer), the properties of which have to be taken into account in the simulations. Superconductor layer thickness is 2 μm, its width is 6 mm, thickness and width of the Ag elements in the simulations are the same as of the superconductor thin film, and thickness of interfacial layers is 40 nm. Crystallographic c-axis of the YBaCuO-layers is parallel to y-axis of the overall coordinate system.

2.3 NbTi Superconductor Filament

The numerical simulation is applied also to NbTi filaments. Radius of the cylindrical filaments is about 30 μm. The filament is embedded in a cylindrical, 5-μm-thick, standard matrix material (here Cu). In a multifilament wire, each filament thus is separated from its neighbours by at least 10 μm. A target spot indicates location of a disturbance. Radius of the target spot is $r_{\mathrm{Target}} = 6$ μm. Without loss of generality, the disturbance is modelled as a surface source. A single heat pulse onto the NbTi of in total 2.5×10^{-10} Ws shall be distributed, as a thermal disturbance of $\Delta t_P = 8$ ns duration; the pulse is distributed over the target radius. Cooling is with LHe. In this conductor, the disturbance thus does not result from a fault current.

3 Phase Transitions in the Superconductors

Phase transitions have to be studied in addition to the simulations of current transport in the three superconductors (BSCCO, YBaCuO and NbTi). This is to support interpretation of the results obtained with these systems near their critical temperature. While it is just one detail of the analysis of phase transitions that will be consulted in Sect. 6.3, namely the order parameter, simulation of the density of electron pairs is necessary to decide how zero loss current transport can be correlated to this density, and to which extent even a fault current, as a disturbance, could be satisfied.

Phase transitions can be classified into first-order and continuous transitions (the latter comprise second order transitions). Under first-order transitions like melting or freezing, the two phases co-exist, with clearly defined phase boundaries, until the transition is completed. In quantum phase transitions, the phases are not spatially separated but in momentum space.

Continuous phase transitions are described by order parameters; these are thermodynamic quantities that in the disordered phase on the average are zero. In continuous phase transitions, the transition point is the so-called critical point.

Standard phase transitions occur at finite temperature and result from competition between energy and entropy of the system. Quantum phase transitions, too, are interpreted as competitions, but now between ground states at $T = 0$ of a many-body system (for example, an ultra-cold gas). Study of phase diagrams at $T = 0$ might hold a key to unsolved problems. We will in Sect. 6.3 consider quantum phase transition just with respect to their order parameter diagram.

4 Calculation of Flux Flow Losses

4.1 Concept

Origin and mechanism of flux flow losses have been described in standard literature, compare e.g. Sect. 7.3 in [10] or Sect. 6.5.2 in [11]. For simulation of the flux flow resistivity, we refer to the previous paper [12] in which a cell model was applied (suitable to both BSCCO and YBaCuO superconductors) and derivation of a new flux flow resistivity model was thoroughly described. The "new" model is essentially a detailed calculation of the electrical resistances in normal conducting, highly diversified solid sub-structures in a superconductor cable including weak links and interfacial resistances. It avoids some questionable assumptions made in traditional flux flow resistance calculations. The flux flow model shall shortly be described in the next subsection. A more detailed description is given in Appendix 3.

Simulation of only substructures of the multifilamentary BSSCO superconductor, like only 1 to 5 of the 91 filaments in the tape, certainly would reduce computation time, but it would not be very helpful for calculation of temperature and current distribution and for stability analysis: We need simulation of the *total* number of filaments in the tape, because it is the surface of the *tape*, not of the filaments, that faces the coolant. The filaments are separated from the coolant (and among themselves) by the Ag matrix, with numerous interfacial resistances due to roughness of the surfaces and contaminations arising from the manufacturing (Powder in Tube) process.

It is not at all clear that each of the filaments in the BSCOO superconductor tape would experience the same transport current and, accordingly, the same potential load: The resistances depend on temperature, which means at least a second-order correction becomes necessary. Only the distribution of disturbances in *all* filaments and thin films, and the corresponding local losses, all in sufficient detail, can reasonably provide current distribution and the temperature field within the total conductor cross section and at the solid/liquid interfaces. All these are needed to correctly simulate current transport and heat transfer.

4.2 How to Numerically Calculate Flux Flow Resistivity and Losses

Flux flow resistances limit current transport when in an experiment with superconductors transport current density exceeds critical current density. Flux flow resistance may come up even if superconductor temperature is below its critical temperature.

Under transport current, losses arising from flux flow resistance will steadily increase conductor temperature if heat dissipation to matrix and coolant are not sufficiently strong. If the

temperature exceeds its critical value, the conductor finally gets into the Ohmic resistance state, which causes even higher losses if current cannot be limited or immediately be commuted to a parallel or conventionally be switched off. The well-known flux creep process will not be considered in this paper.

For calculation of flux flow resistivity, the already mentioned random distribution of superconductor critical temperature, magnetic field and current density [4] around their mean values has been applied, as the first step in this analysis. This idea shall take into account uncertainties that could arise from shortcomings in conductor manufacture. Within the range of random values below the "clean" T_{Crit}, it also reflects an increasing degree of disorder of the charge carriers.

Second, calculation of the flux flow resistivity, ρ_{FF}, of the superconductor grains, as local and time-dependent values, ρ_{FF}(x,y,t), has been made by application of the standard relation, compare again [10, 11]:

$$\rho_{FF}(x,y,t) = \rho_{NC}(x,y,t)B(x,y,t)/B_{Crit}(x,y,t) \quad (2)$$

Strictly speaking, this relation is applicable to the solid (bulk) superconductor, not to a bed of superconductor particles like the grains in filaments shown in part A, Fig. 1c. In order to apply Eq. (2) in a finite element simulation, we accordingly need local values of induction, B(x,y,t), and of upper critical magnetic field, B_{Crit}(x,y,t) *and* of local, normal state resistivity, ρ_{NC}(x,y,t), in a particle bed (the superconductor grains). Very roughly, the ratio B(x,y,t)/B_{Crit}(x,y,t), with B_{Crit}(x,y,t) to be taken a $T = 0$, indicates that the relative superconductor volume occupied by the vortex core is a very small number. In traditional literature, ρ_{NC} frequently is considered a constant, independent of temperature and magnetic field, an assumption that seems to be highly questionable.

If we would intend to model current flow through *individual* grains, a finite element (FE) mesh with extremely fine spatial resolution would be needed. Conductor dimensions are between nanometres (weak link structures), micrometres (grains and filaments) and millimetres (tapes). Mapping each superconductor grain in a tape, and in particular its surface geometry and the weak links, using at least some tens of appropriate elements, inevitably leads to a total element number of nodes and elements by far too large to obtain results within acceptable computation time. It is even not clear that the FE simulation could be successful because of the strongly varying particle (grain, weak link) geometry and the strongly different materials and electrical and thermal transport properties in a tape. Finite element simulations are not infallible.

Instead, not individual grains and their surfaces have been modelled but the FE model applied in this paper is focused onto a *continuum*. This approximation assumes an agglomerate of a very large number of very small superconductor grains. A cell model is used to estimate the normal conduction resistivity, ρ_{NC}, of this agglomerate as an effective value, ρ_{eff}, to finally calculate by Eq. (2) the flux flow resistivity, ρ_{FF}.

The simulation of the flux flow resistivity, as a *continuum property*, has the enormous advantage that calculation of at least ρ_{NC}(x,y,t) and if B(x,y,t) and $B_{Crit,2}$(x,y,t) can be provided with high spatial resolution, also of ρ_{FF}(x,y,t), become *independent* of details of the meshing in the FE procedure.

The continuum assumption presently appears to be the only manageable way to circumvent extremely long computation times when calculating resistances in the simulations. More detailed description of this model can be found in Appendix 3 to this paper.

Besides excursion with time of local temperature, and of non-transparency of the superconductors, the continuum approximation of flux flow resistivity is the third key for successful numerical analysis.

5 Results of Temperature Field Calculations

It is assumed in the following that the fault due to a short circuit in an electrical network starts at $t_{Fault} = 1$ ms (this is the instant when transport current first rises over nominal current). Compared with previous papers [4–7, 9], where $t_{Fault} = 6.5$ ms, computation time is reduced. Current increase to a fault is simulated as before: Increase to 20 times the nominal value, within 2.5 ms.

Under this condition, a first impression of when a quench might occur is given in Fig. 1 that shows the number N_{Eq} of equilibrium iterations needed by the finite element program to obtain convergence of the temperature field in the series of load steps.

The number N_{Eq} reflects the development with time of transient temperatures obtained in three different runs of the FE program. The calculations apply identical input parameters, start and boundary conditions. Computation time is stepwise increased to approach the instant when phase transition is expected. Results refer to the total tape cross section including all superconductor and Ag matrix elements with their temperature-dependent electrical, magnetic and thermal properties. Results are obtained with $N_{El} = 21528$ elements and, in this case, already with the new flux flow resistance model explained in Appendix 3 (comparison between the results obtained with the traditional flux flow resistance will be shown later).

The significant increase of N_{Eq} at $t \geq 2.6$ ms indicates this is approximately the time when a quench is expected to occur very soon.

Figure 2 shows nodal temperature obtained close to this time when onset of a quench is expected. In comparison with part A, results at $t = 2.51$, 2.52, 2.53, 2.56 and 2.6 ms (from top to bottom) are calculated with a strongly increased number of elements ($N_{El} = 29580$ instead of less than 5000). However,

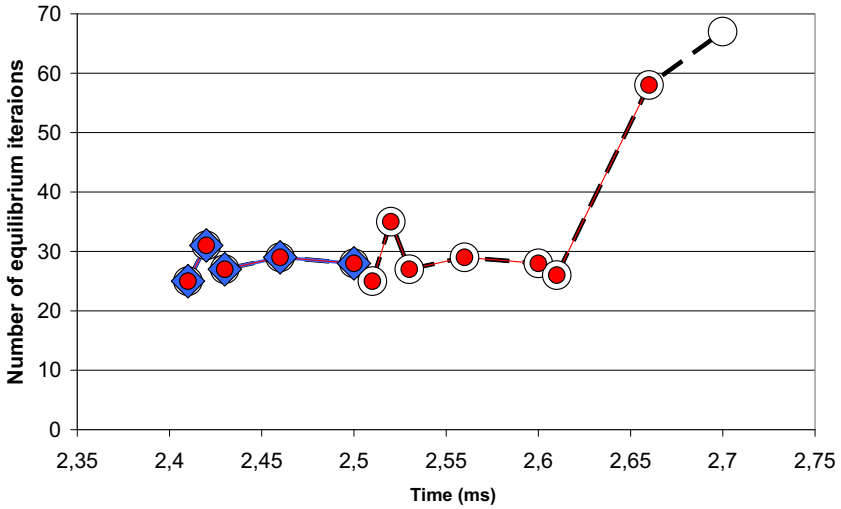

Fig. 1 Number N_{Eq} of equilibrium iterations needed to obtain convergence of the solutions in the load steps of the numerical simulations performed for the multi-filamentary BSCCO 2223 superconductor. The three curves N_{Eq} result from the temperature distribution obtained in different calculations using identical input parameters and steadily increased computation time, either by starting new calculations at $t = 0$ for the full period or by restarts of already converged solutions to approach the instant when phase transition is expected and the superconductor can be prevented from thermal runaway (blue diamonds, solid red circles, open circles). Results refer to the total tape cross section including all superconductor and Ag-matrix elements with their temperature-dependent electrical, magnetic and thermal materials parameters. Results are obtained with $N_{El} = 21528$ elements and with the *new* flux flow resistance model explained in Appendix 3. Note the strong increase of N_{Eq} at $t \geq 2.6$ ms. Extension of the numerical experiment becomes critical since the calculation of the curve with the open circles takes already 18 h (with standard computer equipment)

the consequence of the enlarged number of elements is a strong increase of computation time.

These temperature field calculations have been performed with a conventional value of the flux flow resistivity, about $\rho_{FF} = 10^{-7}$ to 10^{-6} Ω m at small magnetic fields (compare Fig. 17 in Appendix 3). Figure 2 confirms the saw-toothed temperature excursion expected from the temperature vs. time-diagram in Appendix 1, Fig. 13: Compare the schematically shown initial increase of temperature and the following decay in this figure with the corresponding maximum values (right end of the horizontal bar), from 93.624 to 110.159 K during $2.5 \leq t \leq$ to 2.52 ms, then followed by temperature decay from 110.159 to 104.34 K during $2.52 \leq t \leq$ to 2.6 ms, all in Fig. 2. Also, the example shown in Fig. 14 confirms this expectation.

When the calculations, with the same number N_{El}, tentatively are extended to $t = 2.62$ ms, to more closely approach a possibly existing critical time, the point of no return mentioned in part A, reduction of computation time becomes necessary. With $N_{El} = 29580$, the FE program needs about 32 h computation time on a standard PC with 4-core processor and 8 GB working space, to obtain convergence of the results in about 30 load steps and in the total number of about 130 sub-steps.

The number N_{El} therefore was reduced to 22680 elements. Nodal temperature within some of the filaments (a detail of the complete tape cross section) is shown in Fig. 3a and is calculated in steps Δt of 0.1 and finally of 0.02 ms, without significant loss of accuracy against Fig. 2. Results are given for filaments closely located to the symmetry axis of the tape.

Figure 3 a and b demonstrates that there is not only an inhomogeneous temperature field within the total *tape* cross section (trivially, this is expected and was observed already in previous papers and in part A), but the point is that clear non-uniformity of the temperature field is observed also within *individual* filaments.

The bottom diagram in Fig. 3a in addition indicates that temperature apparently splits into two maxima near the centre of the individual filament cross sections. This spatial variation is shown in more detail in Fig. 3b, with $N_{El} = 22680$ (top) and 21528 elements (below). The variation of local temperature is observed in *all* filaments and is *independent* of the total number of elements in the (mapped) meshing scheme.

This is apparently the consequence of a more and more diversified, thermal excitation of the superconductor grain material. From the numerical simulation aspect, the excitation is subject to the interacting thermal and electrical transport and magnetic field penetration processes within the grains that all depend on temperature. But it is also the self-amplifying divergence mechanism, when the system approaches its critical temperature, which is behind the strong temperature distributions, together with strong non-linearity of the transport parameters.

Temperature excursion, $T(x,y,t)$, extracted from Fig. 3b (upper diagram) is shown in Fig. 4b for a single filament (filament 2, compare Fig. 4a for identification of the filament position). Results are calculated with $N_{El} = 22680$ elements again using conventional flux flow resistivity values. Data are taken along the axis of symmetry of the tape, $x =$ 1.92 mm. Temperature is more or less continuous (rather

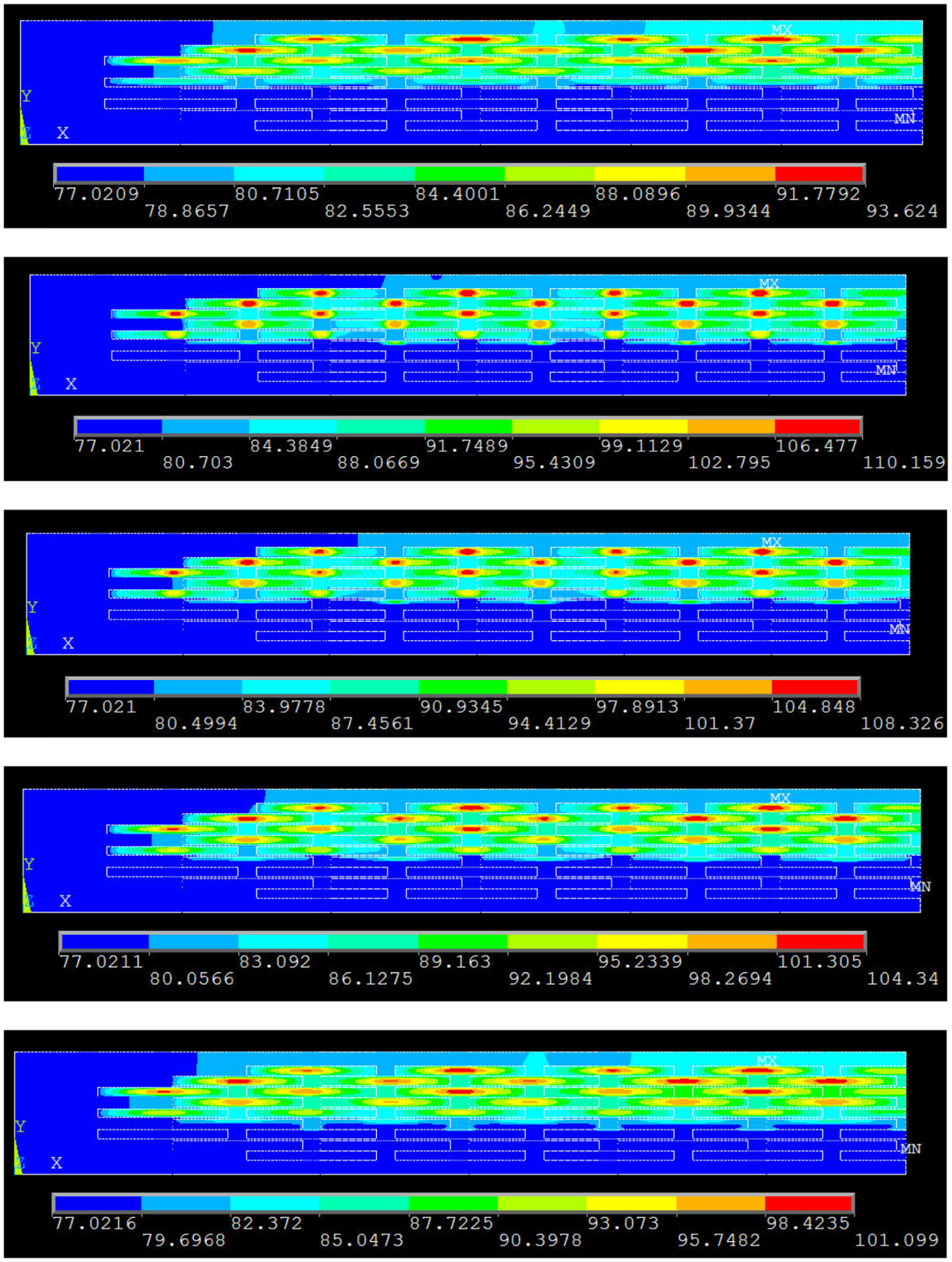

Fig. 2 Nodal temperature in the BSCCO 2223 tape, as expected in situations close to onset of a quench; results are calculated with $N_{El} = 29580$ elements at $t = 2.51$, 2.52, 2.53, 2.56 and 2.6 ms (from top to bottom) and with the traditional flux flow resistivity. Computation time exceeded 32 h

unchanged at $t = 2.6$ and 2.614 ms), but note the sudden increase between 2.614 and 2.62 ms to values all above T_{Crit}.

Temperature excursion within the single filament 1 located in the upper region of the tape cross section is

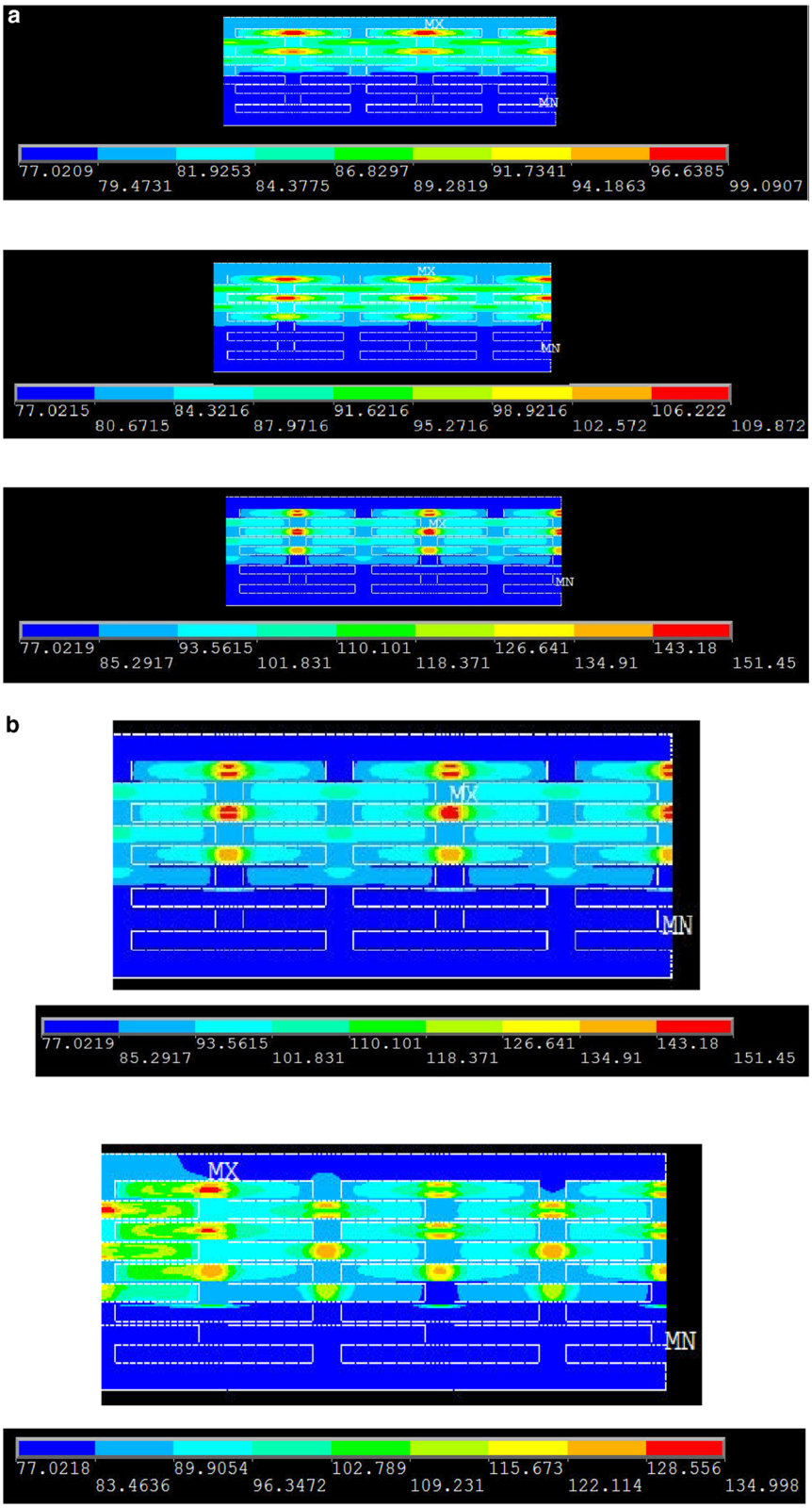

Fig. 3 **a** Nodal temperature (detail) within outermost right elements near the axis of symmetry calculated at 2.5, 2.6 and 2.62 ms (from top to bottom), with $N_{El} = 22680$ elements and again with the traditional flux flow resistivity. **b** Nodal temperature distribution in the tape (detail). Upper diagram: Results obtained with $N_{El} = 22680$ elements and with the *traditional* flux flow resistivity values. Lower diagram, for comparison: $N_{El} = 21528$ elements calculated with the *new* flux flow resistivity model explained in this paper; see text and Appendix 3. Results are given at $t = 2.62$ ms. Although less pronounced in the lower diagram, temperature splits in the centre of the filaments into two peak values, or at least strong temperature variations are observed with application of both schemes. A decision which model is to be preferred can be made only on the basis of experiments

shown in Fig. 4c. Again, strong variation of temperature within the filaments is obvious for all $t \geq 2.6$ ms.

While these calculations (Fig. 4b, c) applied *conventional* values of the flux flow resistivity, results of the same calculation, now with $N_{El} = 21528$ and with the *new* flux flow resistivity model (explained above and in more detail in Appendix 3), are shown in Fig. 5. It again shows strong variations of element temperature. As

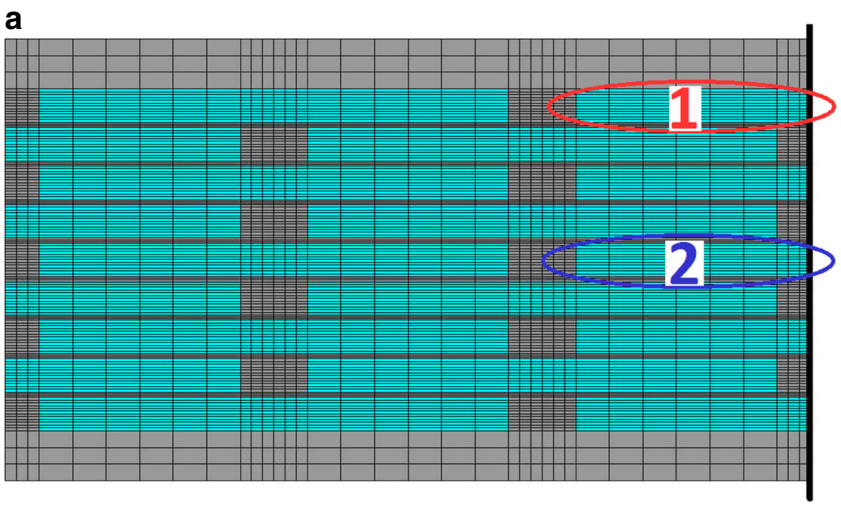

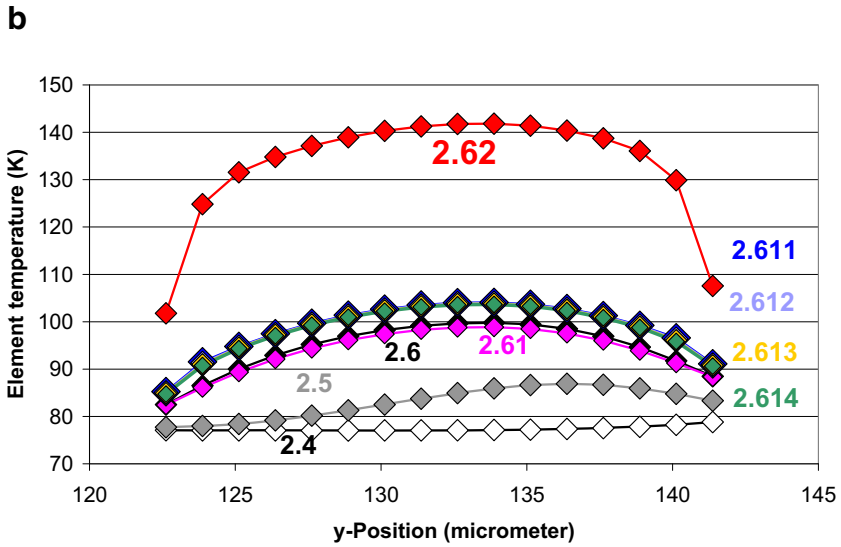

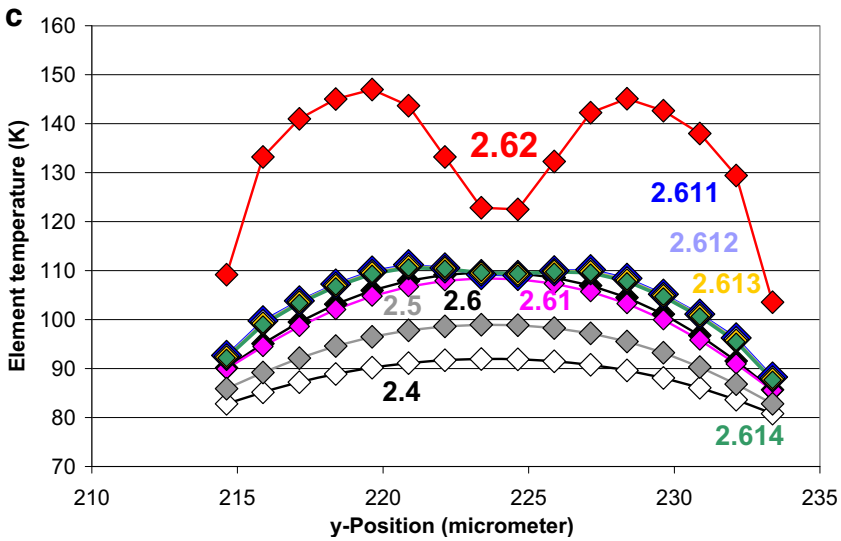

Fig. 4 **a** Part of the total tape cross section showing filaments (dark-green) and matrix elements (dark-grey) and the plane element mesh (mapped meshing). The thick solid line at the right denotes the axis of symmetry of the tape (x = 1.92 mm). Left half, axis-symmetric parts of two single filaments, 1 and 2, are indicated by the coloured ellipses to indentify the tape sections within which temperature distributions and the stability function will be shown in the subsequent figures. **b** Element temperature, T(x,y,t) (arithmetic mean of nodal temperatures),within the *single filament* 2 (compare Fig. 4a to identify filament position in the tape). Element temperature is plotted vs. y-position (with the corresponding x-positions of filament 2 kept constant) along the axis, x = 1.92 mm, of symmetry of the tape. Results are calculated with N_{El} = 22680 elements using the *traditional* flux flow resistivity value (like in Fig. 3b). Vertical position of filament 2 is in the central region of the tape cross section where no splitting of the temperature is observed. Temperature remains more or less continuous (is rather unchanged at t = 2.6 and 2.614 ms), but note the sudden increase between 2.614 and 2.62 ms to values all above T_{Crit}. After a small, additional time-step, a quench would be expected to occur immediately within this filament. **c** Element temperature T(x,y,t) as before (**b**) (arithmetic mean of nodal temperatures) within *single filament 1* (compare **a** for its position). Element temperature is plotted vs. y-position along the axis, x = 1.92 mm, of symmetry of the tape. Results are again calculated with N_{El} = 22680 elements using the *traditional* flux flow resistivity value (like in Fig. 3b). In this diagram, the curves demonstrate splitting of the element temperature at all $t \geq$ 2.6 ms (compare text). Like in **b**, after a small, additional time-step, a quench would be expected to occur immediately within this filament

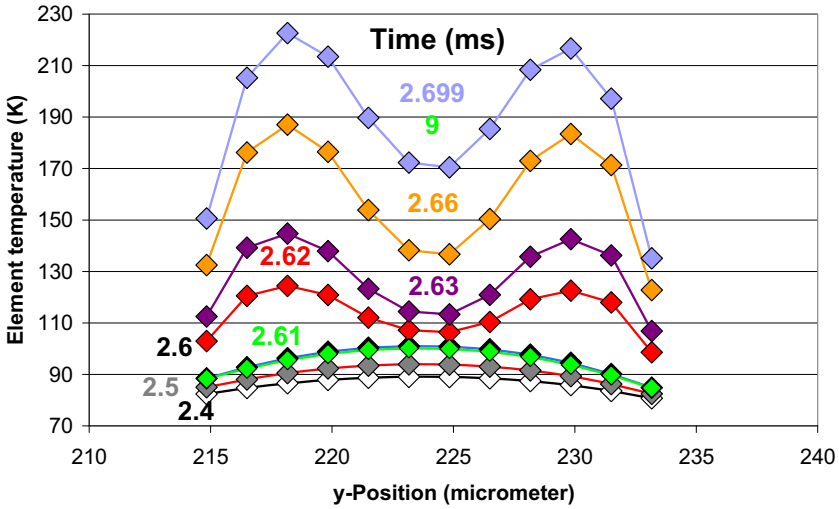

Fig. 5 Element temperature within the *single filament 1*, all at $x = 1.92$ mm (axis of symmetry of the tape; compare Fig. 4a for filament position). The filament is located in the upper region of the tape cross section. Results are calculated with $N_{El} = 21528$ elements and with the *new* flux flow resistance model explained in Appendix 3. The curves as before demonstrate splitting of the element temperature, here at $t \geq 2.62$ ms

before, now with the different N_{El} and with the different flux flow resistivity model, local temperature again splits into two maxima, like in Fig. 3a, b. The significant temperature variation within a filament does not depend on the number of elements or on the model to calculate flux flow resistivity.

The fast increase of the filament temperature at $t \geq 2.6$ ms in Fig. 4b, c indicates that a local quench is soon to be expected, probably after only a small, additional time-step.

We will now concentrate on calculation of stability functions. It is a tool that is frequently applied in stability analysis and might constitute an alternative to only inspection of temperature distributions in the conductor. The stability function reads, with the integral taken separately over numerator and denominator,

$$0 \leq \Phi(t) = 1 - (1/A) \int J_{Crit}(x,y,t)dA / J_{Crit}(x,y,t=0)dA \leq 1 \tag{3a}$$

and over A, the total superconductor cross section. Definition of a stability function apparently originates from [3].This is approximated by

$$0 \leq \Phi(t) = 1 - \Sigma J_{Crit}[T(x,y,t), B(x,y,t)]\Delta A / \Sigma J_{Crit}[T(x,y,t), B(x,y,t_0)](x,y,t)]\Delta A \leq 1 \tag{3b}$$

with the summations taken over all superconductor elements and using their individual cross sections, ΔA.

The ratio J_{Crit}(x,y,t)/J_{Crit}(x,y,t = 0) gets Φ(t) close to zero if J_{Crit}(x,y,t) is close to J_{Crit}(x,y,t = 0), in other words, if the temperature field and thus critical current density are not very different from their initial values. In this case, almost the whole conductor cross section is open to zero loss current transport, with high critical current density (this simplified calculation and interpretation of $\Phi(t)$ neglects losses by flux flow, however). If T(x,y,t) becomes close to T_{Crit}, the critical current density, J_{Crit}(x,y,t), is very small at these positions, and $\Phi(t) \rightarrow 1$. Zero loss current transport then is hardly possible:

$$I_{Transp}(t) = J_{Crit}(x,y,77\ K)A[1-\Phi(t)] \tag{4}$$

If T(x,y,t) > T_{Crit}, we are finally in the Ohmic resistance regime and $\Phi(t) = 1$, which means $I_{Transp}(t)$ without losses is zero because J_{Crit}(x,y,t) is zero.

For the calculation of $\Phi(t)$ by Eq. (3a, b), an integral view of the temperature distributions, in a properly chosen superconductor cross section, has to be taken. Within the said hierarchy (grains, filaments, tape, cable), we tentatively start with total tape cross section involving all filaments.

Figure 6 a shows nodal temperature within the tape calculated at $t = 2.6999$ ms (as will be shown later, a situation very close to the expected phase transition in many filaments of this tape). "Tentatively" means that the calculation of $\Phi(t)$ might be misleading because of the very large temperature variations observed in the tape cross section (Fig. 6a) and, correspondingly, by the large temperature gradients (Fig. 6b).

Large temperature gradients emphasize large local heat transfer rates, and the temperature gradients are responsible for thermal stresses within the superconductor grain volumes and, to a much smaller extent, in the Ag matrix.

The temperature variations, between 77 and almost 290 K, exceed the values seen in all temperature diagrams shown in the previous Figs. 2a and 3a, b and in the temperature vs. y-position diagrams in Figs. 4b, c and 5. But there are also many filaments, about 1/3 of all, of which the temperature is clearly below critical temperature (and even close to 77 K). Critical current density of these filaments thus remains close to the initial value, J_{Crit}(x,y,T = 77 K), and current redistribution and sharing, among

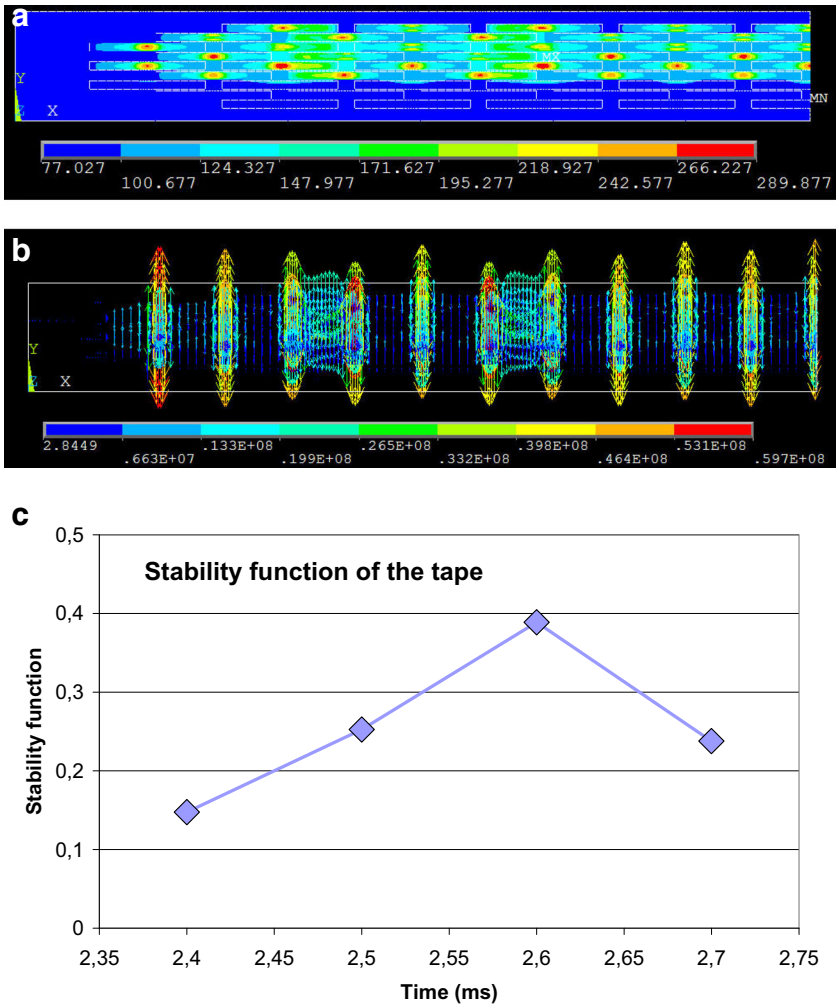

Fig. 6 **a** Nodal temperature distribution within all elements of the total tape cross section. Results are calculated for $t = 2.699$ ms, with $N_{El} = 21528$ elements and with the *new* flux flow resistance model explained in Appendix 3. The overall strong temperature variation including all superconductor elements of the tape is hardly suitable for calculation of the stability function, $\Phi(t)$, see **c**. **b** Gradient of the temperature field, **grad**(T) [K/m], within all elements of the total tape cross section. Results are calculated at $t = 2.699$ ms, with $N_{El} = 21528$ elements and with the *new* flux flow resistance model explained in Appendix 3. The increased density of the arrows between 0.1998e8 and 0.265e8 and between 0.332e8 and 0.398e8 results from the locally finer (horizontal) division of the mesh between adjacent filament positions. **c** Stability function, $\Phi(t)$, calculated using Eq. (3a, b) and the critical current density from **a** of all elements located within the total tape cross section. Note that $\Phi(t)$ is substantially below the critical value $\Phi(t) = 1$ though the maximum values of nodal temperature seen in **a** have increased up to almost 290 K. The explanation is that there are many elements in the cross section (about 1/3 of all), the temperature of which still is below critical temperature, or is even near 77 K

the filaments in the tape, from high-resistance filaments to these low-temperature filaments, will be observed.

The stability function, under the given temperature distribution, then is expected to be small and could even decrease with time if current redistribution and sharing become strong. This is confirmed in Fig. 6c (note the decrease of $\Phi(t)$ beginning with $t = 2.6$ ms).

As reported in our previous papers, this is another example in which the stability function cannot identify regions (and thus does not exclude their existence) in the present tape cross section, or in a superconductor in general, when run-away of local temperature might occur. As a tool to correctly predict stability of superconductors, the stability function works only if temperature differences in the conductor cross section are small. Under a disturbance, originating, e.g. from a circuit fault, this is with multi-filamentary superconductors like BSCCO 2223 not the case, compare Fig. 6a.

The popularity of the stability function apparently goes back to its application to LHe cooled superconductors where temperature variations in the conductor cross section are much smaller, because of the large thermal diffusivity of metals and alloys.

Accordingly, in order to proceed with the analysis of a possible correlation between stability and density of electron pairs, and to make another attempt to successfully exploit the stability function and demonstrate its beyond doubt valuable prediction potential, we have to look onto

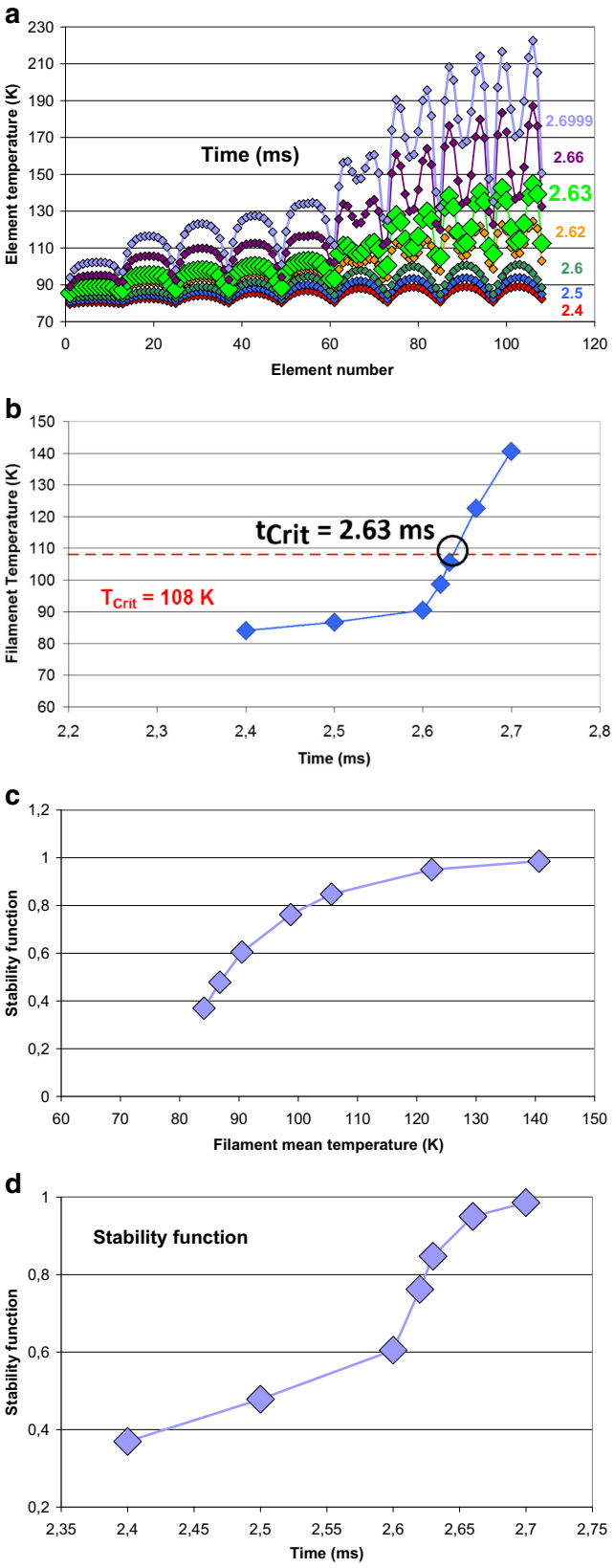

Fig. 7 **a** Distribution of local element temperature of all elements that belong to filament 1 (for filament position in the tape again compare Fig. 4a). Results are calculated with $N_{El} = 21528$ elements and with the *new* flux flow resistance model explained in Appendix 3. For all element numbers greater than 60 and if $t \geq 2.6$ ms, temperature splits into two maxima. At the other positions, the diagram is similar to Fig. 15b in part A, but here with finer resolution. Enlarged symbols for a critical time, $t_{Crit} = 2.63$ ms, with strong fluctuations, indicate that this is apparently the instant when the temperature of a large number of elements is expected to exceed $T_{Crit} = 108$ K. **b** Filament mean temperature (arithmetic mean taken over *all elements of the single filament 1*), vs. time. The figure serves to identify a "critical time" t_{Crit} after which a quench is expected to inevitably occur after additional time steps. **c** Stability function, $\Phi(t)$, between 2.4 and 2.6999 ms, of the *single filament 1*. Results are calculated as before (**a**) but plotted against filament mean temperature. **d** Stability function, $\Phi(t)$, between 2.4 and 2.6999 ms, of the *single filament 1* located in the upper region of the tape close to the axis of symmetry. Results are calculated using Eq. (3a, b) with the $J_{Crit}(x,y,t)$ of all element belonging to filament 1, $N_{El} = 21528$ and the *new* flux flow resistance model explained in Appendix 3. The sudden rise of $\Phi(t)$ between $t = 2.6$ and 2.62 ms indicates the system (the single filament 1) more and more approaches a quench. That the curve in its upper parts shows slight bending towards less than linearly increasing values of $\Phi(t)$ indicates transport current is increasingly dispersed to other filaments within the tape (and, finally to the Ag-matrix)

the next lower (physical) level in the said hierarchy; this level is set by the filaments, the smaller, compact physical unity in the tape cross section. Though there are local positions where temperature remains near the initial value, we can expect, in this second, again tentative step, that the temperature variations and, correspondingly, the temperature gradients, within a single filament are smaller than those calculated over the whole tape cross section. The predictions by the stability function thus will become more convincing.

We consider again the single filament 1. Figure 7 a shows temperature calculated between $2.4 \leq t \leq 2.699$ ms, again with $N_{El} = 21528$ and the new flux flow resistance model. For all element numbers greater than 60, the temperature clearly shows a tendency to split into two maxima (at the other positions, the diagram is similar to Fig. 15b in part A, but is calculated here with finer resolution). A "critical time", t_{Crit}, can roughly be estimated from Fig. 7a when element temperature in this filament starts to strongly fluctuate; this happens at about $t = 2.6$ ms.

This estimate of critical time can be improved: The observed, reduced scattering of the temperature within the filament allows to continue the analysis with a mean filament temperature, $T(x,y,t)$, as is plotted in Fig. 7b. When $T(x,y,t)$ crosses $T_{Crit} = \text{const}$, a sudden increase of $T(x,y,t)$ is observed that allows to identify the critical time as $t_{Crit} = 2.63$ ms, the start of a run-away within the single filament 1 of superconductor temperature.

Calculations of the stability function can be performed up to temperatures very close to T_{Crit}, but the J_{Crit} in the denominator of Eq. (3a, b) must be non-zero.

Though Fig. 7b still delivers just an estimate (because of application of a mean filament temperature), it is confirmed by the stability function (Fig. 7c, d) calculated in the reduced

cross section. Calculation of $\Phi(t)$ is made with only the J_{Crit}(x,y,t) of the elements that belong to this single filament.

First, Fig. 7c shows the (smooth) behaviour of $\Phi(t)$ that is to be expected from the decrease of $J_{Crit}(T)$ with increasing temperature. The sudden increase of $\Phi(t)$ at $t = 2.63$ ms (Fig. 7d) then is in parallel to the estimate of the critical time, t_{Crit}, made in Fig. 7b using the mean filament temperature (and confirms Fig. 1).

The curve $\Phi(t)$ in Fig. 7c, in its upper parts, shows slight bending; it does no longer increase linearly from values obtained at lower filament mean temperature. This observation can be understood from transport current being increasingly dispersed to other filaments in the tape and finally to the Ag-matrix, which reduces superconductor resistivity, load and filament temperature and thus increases critical current density, J_{Crit}(x,y,t) in Eq. (3a, b).

Results obtained with other filaments of the tape would be similar. Since conductor temperature at the lower positions of the tape is smaller, the stability functions calculated for those filaments are smaller, too, because of the larger J_{Crit}. The stability function for these filaments then would be below the $\Phi(t)$ shown in Fig. 7c, d for the single filament 1; the results are an upper limit of $\Phi(t)$.

Based on these results, we will compare the results of item (1) and (2),

1. The results for the stability function obtained from only one single filament like in Fig. 7c, d
2. The development of local temperature (Fig. 7a)

with the results of the second step announced in Sect. 1.1, namely predictions obtained from the microscopic stability model (item 3), i.e. density and decay rates of electron pairs and their comparison with the density of electron pairs necessary to support J_{Crit} (Fig. 8a, b; Table 1).

In summary of this Section, application of the stability function, Eq. (3a, b), certainly provides helpful results to encircle a phase transition, but the method has disadvantages: Highly diversified conductor temperature leads to strongly varying values of local critical current density. In the present examples, it would take too long computation time to arrive at a situation where $\Phi(t)$ finally gets close to $\Phi(t) = 1$. Information on individual hot spots developing in the conductor cross section gets lost. It appears that calculation of $\Phi(t)$ in such situations should be limited to individual filaments. While a quench if encircled by this method would be a local phenomenon (observed in one filament), it is yet of practical value: If just one filament quenches, operation of the tape as a whole already gets into danger, and it is not clear that the heat always can be dissipated in due time to the Ag-matrix or to neighbouring filaments.

Inspection of transient conductor temperature distribution thus appears to be better suited for stability analysis than the stability function, under the given conditions. The alternative to both methods is described in the next section.

6 Limitation of the Numerical Solutions

6.1 Density of Electron Pairs to Support J_{Crit} in BSCCO 2223

The number of electron pairs must be sufficiently large to provide zero loss current transport and to successfully screen the interior of the superconductor against an external magnetic field. Fortunately, even a tiny fraction of the electrons that condensed to electron pairs can be sufficient. All currents in the superconductor, transport and also screening currents flow with critical current density, J_{Crit}.

If we restrict the interesting temperature interval, within which the calculations shall be performed, to $100 \le T < T_{Crit} = 108$ K for BSCCO 2223, the density of electron pairs, $n_S(T)$, must satisfy the said minimum condition in dependence of the abscissa (temperature) values in Fig. 8a, b. This minimum density is obtained from

$$J_{Crit}(T) = J_{Crit}(T = 4K)\ (1 - T/T_{Crit}) = n_S(T) v_{Fermi} 2e \qquad (5a)$$

with $J_{Crit} = 3.75 \times 10^8$ A/m^2 at 77 K, or for YBaCuO 123 the approximately quadratic temperature dependence, $J_{Crit}(T) = J_{Crit}(T = 0)\ (1 - T/T_{Crit})^2$, with v_{Fermi} the Fermi velocity and e the elementary electrical charge.

The Fermi velocity in BSCCO 2223, about 2.86×10^4 m/s, is given by

$$v_{Fermi} = \pi \xi_0 \Delta(E = 0)/h \qquad (5b)$$

with ξ_0 the coherence length in the ab-plane, $\Delta E(T = 0)$ the energy gap, and h denotes Planck's constant. The density, $n_S(T)$, not only must be stable (though in dynamic equilibrium), but the ratio $f_S = n_S(T)/n_S(T = 4\ \mathrm{K})$ at $T = 100$ K must be at least in the order of 10^{-5} of the $T = 4$ K value (n_S is estimated from the electron density of about 6×10^{27} 1/m^3 of which about 1/2 is considered as available for electron pair formation).

The density $n_S(T)$ is obtained as described previously [13] in a model. When this model was suggested, it was called a microscopic stability model because it considers stability not in terms of energy balances or stability functions and thus of critical current density that all are macroscopic quantities. Instead, it addresses the existence of elementary (microscopic) carriers of electricity in the superconducting state.

Results are shown in Fig. 8a. As with the previously investigated YBaCuO 123 superconductor (compare again [13]),

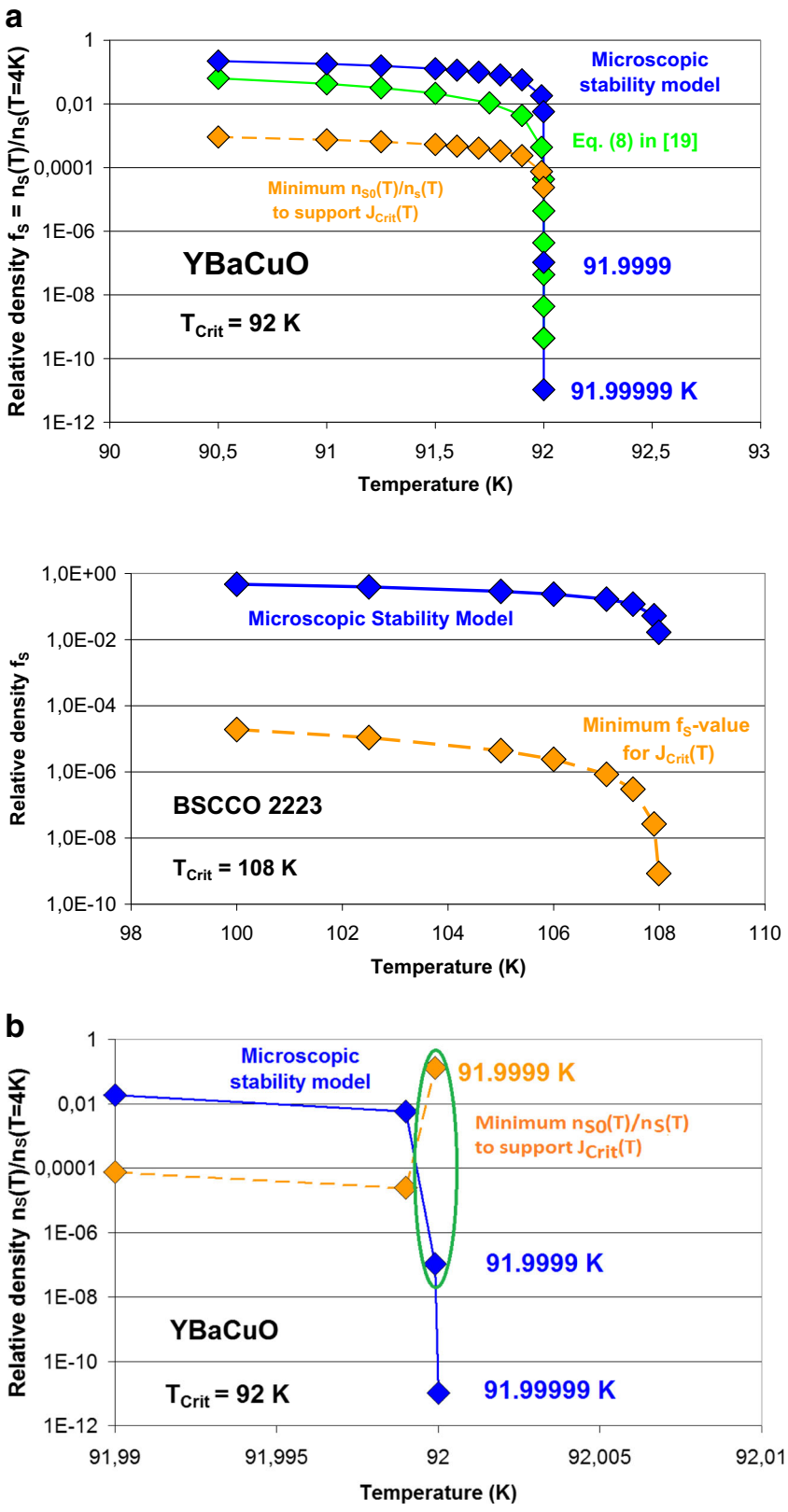

Fig. 8 **a** Relative density $f_S = n_S(T)/n_S(T = 4\ K)$ of electron pairs (the order parameter, f_S), in dependence of temperature, calculated for YBaCuO 123 (above) and BSCCO 2223 (below). Dark-yellow diamonds in both diagrams are calculated as $f_S = n_{S0}(T)/n_S(T)$ thus indicating the minimum relative density of electron pairs that would be necessary to generate a critical current density of 3×10^{10} A/m^2(YBaCuO) and 3.75×10^8 A/m^2 (BSCCO), both at 77 K, in zero magnetic field. The upper diagram is taken from [13]; it also compares predictions of the microscopic stability model (dark-blue diamonds) with results from Eq. (8) in [19] (light-green). **b** Relative density $f_S = n_S(T)/n_S(T = 4\ K)$ calculated like in **a**. The figure shows a detail of the results obtained for YBaCuO 123 with $J_{Crit} = 9 \times 10^{10}$ A/m^2 at $T = 4$ K. The curves are calculated from the microscopic stability model (dark-blue diamonds). The dark-yellow diamonds are obtained as $f_S = n_{S0}(T)/n_S(T)$ using Eq. (5a b,); this is the minimum relative density required to support a given $J_{Crit}(T)$. The green ellipse that encloses the relative densities, both calculated at $T = 91.9999$ K, indicates that the density of electron pairs at this and at higher temperatures (close to, but below T_{Crit}) is too small (the difference $n_S(T) - n_{S0}(T)$, at $T > 91.9999$ K, becomes negative) to support the given $J_{Crit}(T)$; see Table 1

the *required* density $n_{S0}(T)$, dark-yellow diamonds in both diagrams, is small against the *available* density ($n_S(T)$, dark-blue) of the BSCCO 2223 system. Zero loss current transport thus is confirmed.

The ratio (at least 100) between the f_S indicated by the dark-yellow and dark-blue (or light-green) diamonds in Fig. 8a shows that even the assumed fault (a multiple of 20 of nominal transport current) could in principle be satisfied by the density of electron pairs, but flux flow resistance and losses would immediately increase conductor temperature to values above critical temperature and decay of the electron pairs.

The $n_S(T)$, dark-blue and dark-yellow symbols in Fig. 8a (upper diagram) coincide only very late (very close to T_{Crit}), but coincidence yet can be identified. But when $T_{Crit} - T < 10^{-4}$ K, calculation of the (residual) $n_S(T)$ by application of the microscopic stability model to the other conductor, BSCCO 2223 (lower diagram), the calculation becomes more and more time consuming and finally takes too long to arrive at a useful result.

This is explained as follows: In a series of individual reorganisation (decay and recombination) steps under dynamic equilibrium conditions, described using the fractional parentage scheme of this model, the very long computation time is the consequence of the increasingly large number of electrons that are involved in these re-ordering processes: If an arbitrary electron pair composed of electrons i and j (of a total number N_{Ep}) decays to separated, single particles, all N_{El} separated, single electrons have to be reorganised to obtain a new dynamic equilibrium state. Time needed for reorganisation thus depends on N_{El}. The closer T approaches T_{Crit}, the larger is the number N_{El} that has to be re-ordered. Re-ordering has to fulfil the Pauli principle.

Going back to Fig. 1, a simple straight-ahead, alternative method was reported to at least estimate the critical time when in the multi-filamentary BSCCO 2223 superconductor, a quench is expected: It is the number N_{eq} of equilibrium iterations. The curves in Fig. 1 run in parallel to and thus are confirmed by the results reported in Fig. 7a–d.

6.2 Density of Electron Pairs to Support J_{Crit} in YBaCuO 123

The situation is better with YBaCuO 123: Fig. 8a, b shows both densities at temperature values very close to T_{Crit} (92 K). The curves coincide at about the distance $\Delta T = 10^{-4}$ K from T_{Crit}. The upturn of the dark-yellow diamonds, i.e. $f_S = n_{S0}(T)/n_S(T)$, results from the decrease of $n_{S0}(T)$ that reflects the temperature dependence of J_{Crit}. It is comparatively weak in relation to $n_S(T)$ with its strong exponential dependence on temperature.

Beginning at $T = T_{Crit} - \Delta T$, the available electron pair density finally (Table 1, italic entries) becomes smaller than the density required for zero loss current transport. Under given voltage, the transport current then has to be realised by unpaired, normal conducting electrons. Thus, current has to run against Ohmic resistances, which leads to fast temperature increase. This is reflected by the divergence of the numerical results for $f_S = n_{S0}(T)/n_S(T)$, dark-yellow diamonds in Fig. 8b.

Success of the microscopic stability model thus may depend on computation time; in case of the BSCCO superconductor, computation time becomes too long to observe coincidence. This lack of the method may be avoided with superconductors of smaller T_{Crit} (like YBaCuO). But another problem arises from comparison of the length of load steps and time constants, as will be shown in the next subsection.

6.3 Classification of Phase Transitions

6.3.1 Order Parameters

This subsection deals with phase transitions in superconductors; thus, on systems at $T > 0$, with a very large particle number. For a review of quantum phase transitions ($T = 0$), refer to [21]. The description of an experimental study to approach a quantum phase transition in an ultra-cold gas, from a super-fluid to a Mott insulator, is published in [22]. Both papers are examples taken from the large variety of existing publications in this discipline.

If in a quantum phase transition the system approaches a critical point, spatial correlations of the order parameter become long-ranged distances. Close to this point, the correlation length scale, ξ, over this distance follows $\xi \sim 1/|t|^{\nu}$. If the (continuous) phase transition occurs at $T > 0$, the distance can be written as $t = (|T - T_{Crit}|)/T_{Crit}$. The length ξ thus diverges if $t \to 0$ (ν is a spatial critical exponent, $\nu > 0$). But if the system consists of ordered and disordered phases in parallel, the correlation length will be finite, not exceeding the corresponding spatial dimensions.

In analogy to this *spatial* (long-range) correlation, long-range correlations of order parameter fluctuations also exist in *time*, on a scale $\tau_{Crit} \sim \xi^2 \sim 1/|t|^{(\nu\ z)}$, with z a dynamical critical exponent.

The problem in phase transitions in general is how to determine order parameters and their spatial and temporal dependency.

The microscopic stability model [13] not only describes superconducting to normal conducting phase transitions as continuous transitions, in the vicinity of their critical temperature. The model also might provide a potential tool to calculate order parameters. It applies an analogy to the nucleon-nucleon, pion-mediated Yukawa interaction (here applied to electron-electron correlations during formation of electron pairs), an aspect of the Racah-problem (for expansion of an anti-symmetric N-particle wave function from a $N-1$ parent state), and the Pauli and uncertainty principles, all in dependence of the local (transient) temperature; these approximations are performed in a stepwise, sequential manner for transient temperature fields (those reported in the previous sections). The model takes into account that the stronger the binding of the electron pairs is, the larger the number of states into which during decay the electrons can be scattered.

Interestingly, the relative density, $n_S(T)/n_S(T=0)$, of electron pairs in a virtual unit volume (the Coulomb volume); the time constants, τ_{El} and the decay rates, $d[n_S(T)]/dt$, in this model either diverge to finite but very large values or they decay sharply to zero, at $T = T_{Crit}$. This is shown for BSCCO, YBaCuO and NbTi superconductors (compare Figs. 8 and 9a, b; the originals are found in [13]). Also, the radius r_C of the virtual Coulomb volume diverges when T approaches T_{Crit}.

Density of electron pairs and their derivative with time, as obtained from calculations using this model, apparently run in parallel to the behaviour of ξ and τ_{Crit} and thus to the order parameter when approaching a critical point in any, including quantum, phase transitions.

While the physical background of the microscopic stability model is strongly different, it is yet tempting to discuss whether a similarity of the results provided by the numerical approach in one system (the microscopic stability model [13] with the order parameter $f_S = n_S(T)/n_S(T=0)$, with τ_{El}, and $d[n_S(T)]/dt$, all with respect to electrons in superconductors at $T > 0$) can be understood from the ξ and τ_{Crit} and the order parameter of the other system, which means standard phase transitions ($T > 0$), or as an extreme case, quantum phase transition at $T = 0$, considering the particles of an ultra-cold gas [22] as an approach to this transition.

If so, why do both systems (their order parameters) culminate in a divergence or in a sharp decay, to infinity or to zero, at a critical temperature or at a critical point, respectively? It is the question of the physics behind.

An attempt has been made to answer both questions in [13]. Figure 9b and the diagram (b) in Fig. 1 of [21], here reproduced

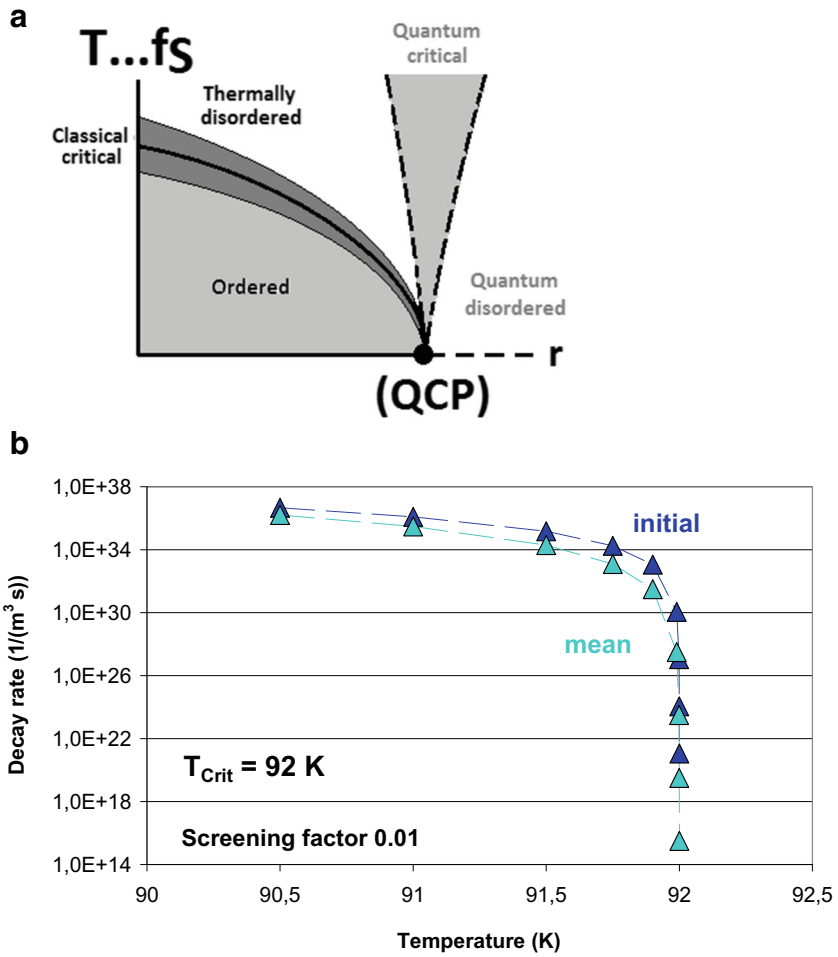

Fig. 9 **a** Phase diagram (schematic) showing two hierarchies: the quantum phase diagram near a quantum critical point (QCP, dashed lines) and the classical analogue (left to the QCP) with the order parameter, f_S, instead of temperature, T. The Figure is redrawn, with modifications (T replaced by f_S), from Fig. 1, part (b) in [21]. The parameter r on the horizontal axis is used as a control parameter to tune the system through the quantum or classical phase transition. The thick, solid line marks the finite-temperature boundary between ordered and disordered phases. Close to this line, the critical behaviour is classical. **b** Initial and mean decay rates (per unit volume) of thermally excited electron states calculated using a screening factor, $\chi = 0.01$, to the Coulomb potential, in a virtual conductor volume, V_C, of the superconductor YBaCuO 123. See text in the original paper [13] and Sect. 6.3 for explanations. The area below the curves corresponds to the ordered phase (electrons condensed to electron pairs) that is from the thermally disordered phase (electrons from decayed electron pairs) separated by the classical critical, finite temperature boundary

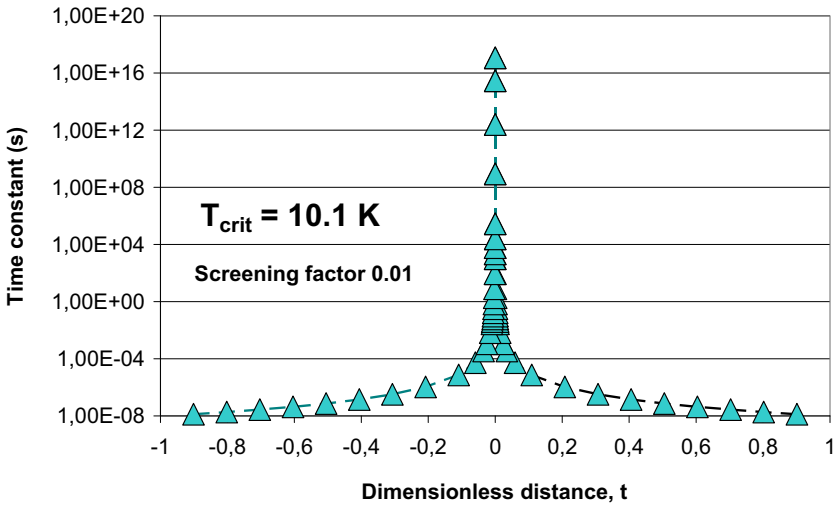

Fig. 10 Time constant (relaxation time) τ_{El} for decay of electron pairs in a superconducting NbTi-filament. Time or time constant, τ_{El}, is to be understood as the relaxation time that the system needs, at a given temperature, T, to complete a phase transition, here after a thermal excitation of the electron system. Results are calculated using a screening factor, $\chi = 0.01$, to the Coulomb potential, in a virtual conductor volume, V_C. See text in the original paper [13] for more explanations. Results are shown in dependence of dimensionless distances, $t = |(T - T_{Crit})|/T_{Crit}$. The distance t is explained in Sect. 6.3 and like in Fig. 9b is used to tune the super/normal conductor system, here by variation of conductor temperature, T, through the phase transition. The right-hand side of the diagram, $t > 0$, cannot be reached by the microscopic stability model; data in this part of the diagram are just mirror images of the corresponding values obtained at $t < 0$. With increasing temperature, $t \rightarrow 0$ ($T \rightarrow T_{Crit}$ from below), it would take the system extremely long to totally complete the superconductor/normal conductor phase transition. In the *simulations*, under a continuing disturbance, the system "jumps" to normal conduction thus leaving a small, residual amount of electron pairs in a small volume within which the phase transition cannot be completed (this is, however, without any significance for resistive current transport). In *physical reality*, there is no jump (time is continuous)

in Fig. 9a, serve to compare both systems and to explain similarity and differences.

6.3.2 Similarity of the Order Parameters in Different Phase Transitions

Figure 9 a reflects the well-known temperature dependency of the Ginzburg-Landau order parameter, $|\psi|$. For comparison of Fig. 9b with Fig. 9a, it is useful to replace

1. Temperature, T, on the vertical axis in [21] by a (physically reasonable) temperature-dependent quantity, here the relative density or the decay rates (Fig. 9b) or the time (Fig. 10). The relative density, $n_S(T)/n_S(T = 0)$, in Fig. 9b thus takes the role of the order parameter
2. The control parameter, r, on the horizontal axis in [21] (there used to tune the system through the quantum phase transition under variations of non-thermal parameters) by the dimensionless distance, t, in Figs. 9b and 10

The region *below* both curves in Fig. 9b (the superconductor) then corresponds to electrons condensed to electron pairs; outside this region, the decay rate is zero (there are no electron pairs within this region). This region (below both curves in Fig. 9b) reflects the region *below* the single (but scattered) curve of the ordered phase in Fig. 9a (the quantum phase transition).

The region *above* both curves in Fig. 9b (the disordered phase of the electrons) then corresponds to the disordered phase (the gas particles) in Fig. 9a: In the superconductor, this concerns electrons that are not, or are no longer, condensed to pairs and therefore are considered as disordered (in this phase, electrons condensed to pairs co-exist with normal conducting electrons). In the quantum system (Fig. 9a), disorder is caused solely by particle statistics (condensed particles co-exist with normal gas particles but are separated in momentum space).

Both regions are separated by the classical critical, finite temperature boundary that in Fig. 9a (solid curve) is given by uncertainties (fluctuations) of the system temperature. Also in Fig. 9b, the boundary is not sharp; this is partly explained by the difference between the curves indicated as "initial" (decay of pairs at the begin of the simulation) and "mean" (taken over the whole period when an increasing number of pairs already has decayed and therefore the decay rate decreases steadily). Another explanation is the statistical variation of critical temperature against its mean value; the random distribution of T_{Crit} (Fig. 16 in Appendix 3) applied in the present calculations enters via the energy gap into this model.

The similarity between Figs. 9a and b therefore results from the curve "finite-temperature boundary between the ordered and disordered phases" (the solid curve in Fig. 9a, and the dark-blue and dark-green diamonds in Fig. 9b; the curve in both systems increases with decreasing temperature, T, or distance, t, respectively.

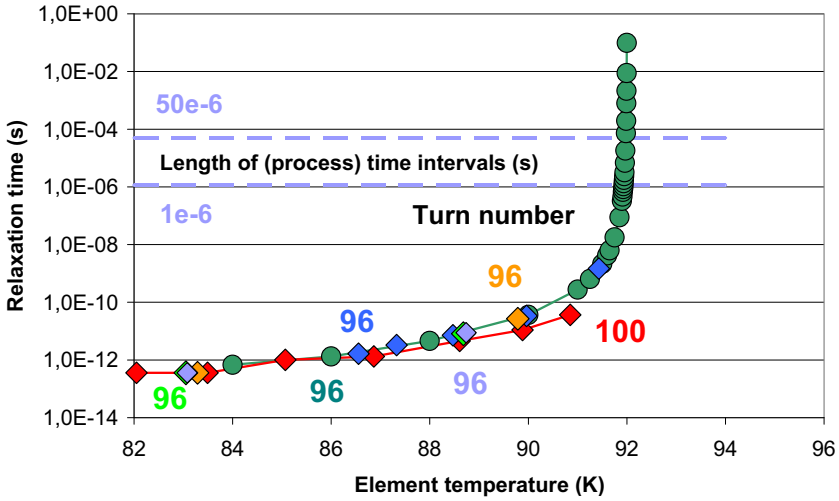

Fig. 11 Relaxation time (the time needed to obtain dynamic, quasi-equilibrium in the centroids of turns 96 (light-green, lilac, orange and blue diamonds, respectively) and 100 (red diamonds) of a coil of coated, thin-film YBaCuO 123 superconductor (in total 100 turns), after a thermal disturbance originating from transport current density locally exceeding critical current density. The light-green, lilac, orange and blue diamonds refer to element temperature calculated in the finite element simulation; dark-green circles are calculated for an arbitrary sequence of element temperatures. Differences of the calculated relaxation times originate solely from the random distances between two electrons in the volume V_C. As soon as element temperature exceeds 91.925 K, coupling of all electrons in this thin film superconductor to a new dynamic equilibrium can no longer be completed within the integration times, here 1 or 50 μs, indicated as length of process time intervals (lilac horizontal dashed lines) in this figure. The figure is taken from [9]

With the above substitutions (1) and (2), the similarity between both Fig. 9a and b also suggests to plot the time constant, τ_{El}, the time needed for recombination of single electrons to pairs, versus the dimensionless distance $t = (T - T_{Crit})/T_{Crit}$ (Fig. 10).

Time constant, τ_{El}, on the t-axis of Fig. 10 is to be understood as the relaxation time that the system needs, at a given temperature, T, to complete a phase transition, here after a thermal excitation of the electron system. But the transition can be completed within a load step *only if* τ_{El} is smaller than the length, Δt, of this step, compare Fig. 11. Since τ_{El} diverges strongly when $t \rightarrow 0$, completion of the transition that involves all particles within Δt becomes increasingly difficult (strongly retarded; see the horizontal lines in Fig. 11) and becomes finally impossible at temperatures very close to T_{Crit}.

This does not mean there is no phase transition at all at temperature very close to T_{Crit}. Assume that during heating, the system arrives at a temperature, T', a value on the abscissa in Fig. 10. The temperature, T', corresponds to a τ_{El} that probably exceeds, Δt, of the load step. Completion of the transition in time then is possible for only a finite part of the electron pairs. The numerical system then proceeds to the next load step where during heating this ratio, $r(T)$, decreases. But since also the density of electron pairs, $n_{El}(T)$, decreases with increasing temperature, the absolute number of non-decayed electron pairs, $r(T)\ n_{El}(T)$, per unit volume becomes small when $T \rightarrow T_{Crit}$.

6.3.3 Numerical Simulations vs. Physical Reality

In the *simulations*, with load steps of finite length, Δt, the system for $t < 0$ under a continuing disturbance (heating) thus "jumps" to the next load step and eventually to normal conduction ($t > 0$) without building (simulating) the quasi-equilibrium state at $t = 0$, and without all electron pairs decayed to single electrons. But the residual electron pairs are without any significance for current transport because their number is too small to support a non-zero J_{Crit}.

Consider in Fig. 10 first the diagram from the left side ($t < 0$, heating): It takes the system of electrons (still condensed to pairs in the virtual volume V_C) with decreasing distance, t (here with increasing $T \rightarrow T_{Crit}$ from below) *the longer* it takes to release the electrons from being coupled to pairs to the disordered state, *the larger* the number N of separated electrons that already occupy this state. This is because the electrons in the equilibrium final states have to obey the Pauli principle and thus may occupy only allowable, single electron states; these have to be identified (which takes considerable time: A very large number of time differentials has to be summed up).

Fulfilment of the Pauli principle therefore is the reason why the total time interval needed to complete this re-ordering (decay of pairs to single electrons) process becomes increasingly large when $T \rightarrow T_{Crit}$. In the calculations, the process has to be repeated for each single step n of the large number N of decay events. The total time interval therefore increases strongly by the very large number of summations over individual time differentials (each about 10^{-13} s).

This result in consequence decreases in Fig. 9b the decay rates when $T \rightarrow T_{Crit}$. An explanation also is given by the strongly decreasing density of electron pairs: The number of electron pairs that could decay goes to zero at T close to T_{Crit} (dynamical behaviour of the system strongly slows down).

The right-hand side of the diagram, $t > 0$, cannot be reached by the microscopic stability model; data shown in Fig. 10 for $t > 0$ are just mirror images of the corresponding values obtained at $t < 0$ (in Fig. 9b, they are simply omitted). With decreasing temperature, $T \rightarrow T_{Crit}$ from above (cooling), $t \rightarrow 0$, it would take the system extremely long to totally (virtually) complete the normal conducting to superconducting phase transition.

In the reverse situation (cooling), again in the *simulation*, the system accordingly jumps from normal conduction to superconductivity ($t < 0$), as before without necessarily building (simulating) a quasi-equilibrium state at $t = 0$. A finite, residual number of unpaired electrons thus remain in the system, but without any significance for disturbing zero loss (zero resistance) current transport.

In the *physical reality*, however, states at $t = 0$ will be build up, since time is a continuous variable (there are no jumps of time that here could be relevant). But there remains a gap between simulation and reality.

Going back to *simulations*, the gap cannot be closed by arbitrarily extending the length, Δt, of load steps or substeps to values always larger than τ_{El}, the electron relaxation time. A complete simulation of the phase transition, until all electron pairs are decayed or all single electron are recombined to pairs, respectively, at $t \rightarrow 0$, from below or above, is not possible in a numerical scheme with finite length of load steps.

A compromise therefore has to be found: When $t \rightarrow 0$, the load step length Δt in the simulations has to be adjusted as to get the product $r(T)\, n_{El}(T)$ in each step as small as possible, the absolute number of not decayed pairs or of not recombined single electrons, respectively.

6.3.4 Combining the Results

We thus have items (1) to (6), arguments that confirm agreement between the curves reported in Figs. 8a, 9a, b, 10 and 11:

1. In Fig. 8a,the dark-blue and light-green diamonds in the upper diagram; the agreement becomes better the more T approaches T_{Crit}, where both values, from quite different models, finally coincide.
2. We also observe qualitative agreement in Fig. 9a, b (the critical points and the curve of the classical critical, finite temperature boundary) and in Fig. 10 (the divergence to very large values of the time constant when $t \rightarrow 0$).
3. With the confirmed (item 2) microscopic stability model, also the curve showing the minimum number of electron pairs necessary to support a critical current density, $J_{Crit} > 0$, is confirmed (Fig. 8a, upper diagram, dark-yellow and dark-blue diamonds),
4. The coincidence of the dark-yellow and dark-blue diamonds in Fig. 8a (upper diagram) and comparison of the last two lines of Table 1 indicate that at a difference of only 10^{-5} K below T_{Crit}, the number of available electron pairs after an additional time step in the simulations no longer would be sufficiently large to support non-zero J_{Crit}. From this time on, current transport is by normal conducting electrons, with correspondingly large increase of the resistance to the Ohmic resistance state (a quench will be the consequence). By the standard Kirchoff resistance network, the simulations do not allow competition between current transport by the small number of residual electron pairs and the normal conducting electrons,
5. This confirms the numerical simulations in [9] of transient temperature in the YBaCuO 123 superconductor (and also of the BSCCO 2223 system and its stability function) in which a strong increase of local temperature after a critical time was observed, which indicates the system is close to onset of a quench.
6. Finally, onset of a quench in the BSCCO 2223 superconductor was already revealed by the maximum number of converged equilibrium iterations (Fig. 1).

6.4 Non-Transparency vs. Time Scales

A corollary from radiative transfer was discussed in [6]: The question is whether physical time and time scales in general are uniquely defined in non-transparent systems.

Non-transparency has been shown in part A of the present paper to be a pre-requisite for validity of the additive approximation. Non-transparency, on the other hand, raises the principal problem of how to interpret time scales in experiments with superconductors when images of the *same* event are created at *different* times after their occurrence, and probably at different positions. This happens because of different, parallel transport channels (phonons, radiation by scattering or absorption/remission and others) that all would interact and that all proceed with strongly different velocity. Among these, transport of thermal excitations by phonons is the slowest part, and scattering of radiation the fastest who leads all others to create images. The bijective correlation that exists in transparent systems between events and images gets lost.

This does not collide with relativity principles. But an answer to this question may have consequences for reliability and predictions of all non-stationary stability models (and also

in other physical disciplines). See [6] for explanations. More results will be published in the future.

7 Current Transport Near the Phase Transition

In retrospect, beginning with the apparently existing parallel between the present results (Fig. 9b, the order parameter) with the spatial and time dependence of the order parameter in quantum phase transitions (Fig. 9a), items (1) to (6) in Sect. 6.3 provide confidence in the numerical, transient temperature field and stability calculations, and they provide confidence also in the search of a correlation between results obtained from the numerical (non-convergence) study and the experimental situation.

The results obtained from the numerical simulations and the microscopic stability model, and items (1) to (6) in Sect. 6.3, all in common lead to the summary Fig. 10 and 11, for the superconductor NbTi filament and the YBaCuO 123 thin film, respectively.

Thus on the one hand, the agreements found in Sect. 6.3 support the numerical results, and in general the working steps of the microscopic stability model [13], for if the numerical steps in this model would be incomplete or seriously be wrong, agreement, neither quantitatively nor qualitatively, not even just a similarity between Fig. 9b with the curve of the classical or quantum critical phase boundary in Fig. 9a, could be expected.

On the other hand, collision between length of load steps and relaxation time can put numerical simulations of current transport in heavy waters, if they are modelled as a series of converged, quasi-equilibrium solutions: Redistribution of transport current that would be completed instantaneously (or at time scales very short against thermal or other time constants) cannot be modelled within load steps or sub-steps of finite length. While the well-known (small) jump of the specific heat at $T = T_{Crit}$ can easily be integrated into the numerical (finite element) procedure, since length of the thermal time constant is *finite* (it is based on the dominating, rather slow phonon component), this is following Figs. 10 and 11 not the case with current transport. Completion of the phase transition at temperatures very close to critical temperature thus superimposes on electricity transport, in a considerable part of the intervals Δt. Numerical simulations of current transport near phase transition thus may become severely in error if length of load steps is too short and thus in conflict with completion of the phase transition.

Within numerical simulations, this conflict apparently cannot be avoided. With the density $n_{El}(T)$ of NbTi calculated in [13], length of load steps and time constant for decay and recombination then are needed to at least minimise the product $r(T)\ n_{El}(T)$.

As a consequence, the bijective correlation mentioned in Sect. 1.2, between spaces (1) and (2), the space of the physical reality and the numerical space, respectively, is the less fulfilled the closer the system approaches critical temperature. The hypothesis set up in Sect. 1.2 thus cannot be fulfilled in general.

All this waits for experiments to be performed with *non-transparent* samples, to confirm the numerical results. Non-transparency and the validity of the additive approximation are the conditions behind the results obtained in the previous sections. Measurements of the time constants could be performed around the phase transition with dynamic (AC) measurements, like in AC magnetic susceptibility experiments; see standard literature, e.g. [23] Chap. VIII; lecture notes on the physics of AC magnetic susceptibility can be consulted in [24].

8 Summary

Numerical simulations have been performed with a multifilamentary BSCCO 2223, a coated, thin-film YBaCuO 123 tape and a NbTi superconductor filament. Under disturbances, here a fault current, the resulting transient temperature distributions in the conductor cross section are strongly non-uniform.

Non-convergence of the numerical scheme might tightly be correlated with onset of the superconductor to normal conductor phase transition. While a rigorous proof of this hypothesis is hardly possible, the results obtained for transient temperature distributions, stability functions and local values of critical current and electron pair density, under continuous increasing, self-amplifying losses in these superconductors, have been shown to allow encircling position and time of the anticipated phase transition from results of a series of load steps; the method, if performed in finite element calculations with highest possible spatial and time resolution, would allow to catch the superconductor on the last metres (milli- or micro-Kelvin) from quenching.

But numerical simulations of current transport near phase transition may become severely in error if length of load steps is in conflict with time needed for completion of the phase transition. This conflict apparently cannot be avoided if the system is close to the phase transition. As a consequence, the hypothesis set up in Sect. 1.2 is not fulfilled in general.

Density of electron pairs vs. phase transition from the superconducting to normal conducting state allow identification of the minimum density, $n_{S0}(T)$, of electron pairs necessary for support of critical current density. It is not only the traditional condition, $T < T_{Crit}$, in standard stability calculations that has to be fulfilled in order to protect the superconductor against quench. Comparison of $n_{S0}(T)$ with the temperature dependent, actual density, $n_S(T) >$

$n_{S0}(T)$, a condition that, strictly speaking, is to be fulfilled at all $T = T(x,y,t)$ during a disturbance, supports and completes decision-making.

Sequential approximations in the numerical calculations and in a microscopic numerical stability model provide a tool for calculation of order parameters, at least in standard finite temperature phase transitions. There is, of course, still the Ginzburg-Landau theory for superconductors as an alternative.

A differentiation between numerical simulation and physical reality becomes more important the more the superconductor approaches critical temperature, when length of load steps in the simulations becomes smaller than relaxation times. Phase transition at temperatures very close to critical temperature superimposes on electricity transport and may have serious impacts, if not completed, on magnitude of current and critical current density and on simulation of current redistribution.

Therefore, stability analysis is not, or not only, a problem of current transport and critical current density but in the calculation of transient temperature fields also relies on understanding of phase transitions and their completion to new dynamic equilibrium.

A final question: Are the calculation steps of the microscopic stability model perhaps suitable also for calculation of order parameters in other standard and possibly also in quantum phase transitions? Additional investigations will be needed to find an answer.

Experimental confirmation of the results obtained in the reported procedures (numerical simulations, interpretation of the phase diagram) might become enormously difficult, which however is the problem of all stability models. But attempts would be highly appreciated. Candidates are dynamic (AC) measurements (performed like in AC magnetic susceptibility experiments) around the phase transition. Experimental confirmation still is not avaiable. Yet the paper shall demonstrate the enormous potential of numerical simulations also of transient superconductor states and of current transport near phase transitions.

Appendix 1. The Numerical Iterative Master Scheme.

The numerical simulations reported in part A (DOI https://doi.org/10.1007/s10948-019-5103-7) and in the present paper apply an iterative calculation scheme (in the following called the master scheme) illustrated in Fig. 12. The master scheme consists of

1. As an inner core, a finite element (FE) program for solution of Fourier's differential equation. In case heat transfer by radiation becomes involved (a problem that may be important to thin films), a Monte Carlo (MC) simulation will be included but is not part of the proper FE procedure. It is needed to provide solutions of the equation of radiative transfer that contribute to the initial conditions of the FE calculations in each load step. FE and MC solutions yield the transient temperature field in the superconductor; this constitutes step (1) of the simulations.
2. Peripheral numerical procedures (that incorporate this core) serve for calculation of local values of critical parameters (current density, magnetic field and its penetration), of the Meissner effect, of local resistance, fault states, electrical losses of the conductor and of distribution of the transport current (steps 2 to 5).

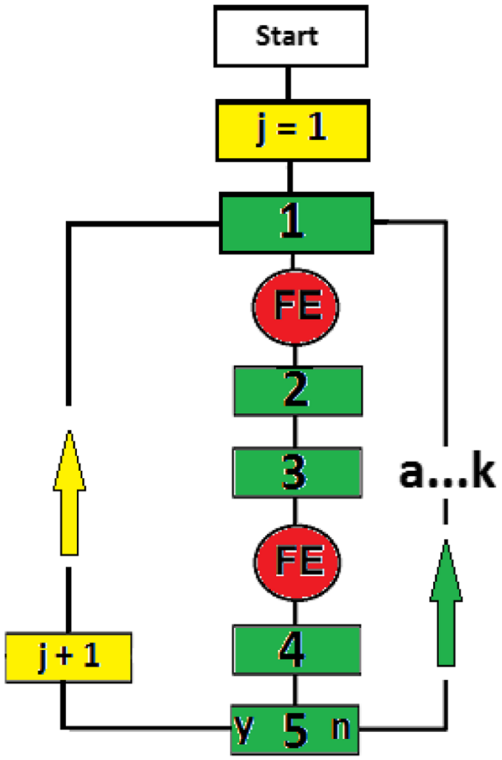

Fig. 12 Flow chart of the numerical simulation procedure. Green rectangles with sub-step numbers 1 to 5 are defined as: **1** If $j = 1$ (first load step), data input of start values of temperature distribution, specific resistances, critical parameters (J, B), transport current distribution I_0; if $j > 1$ (next load steps, after at least two intermediate, converged FE calculations within each of the iterations a...k), application of recalculated temperature, specific resistances, critical parameters, current distribution I_j as the next data input; **2** results obtained after first converged FE step for the same parameters in the *same* load step, calculation of T_{Crit}, B_{Crit}, J_{Crit}; **3** calculation of resistance network and of transport current distribution I_j, all as data input into the next FE calculation within the *same* load step j; **4** results like in **2**; **5** results like in **3**, convergence yes or no? If no, return to **1** (iterations a...k, in the same load step), if yes go to next load step $j + 1$, continue with **1**. The number N_{FE} of FE calculations (red circles within individual sub-steps a...k) is not fixed to $N_{FE} = 2$ but can be extended arbitrarily (but like the number $N_{It} \leq 10$ of iterations a...k strongly increases computation time). Decisions on N_{FE} and N_{It} can be made from observed convergence or non-convergence in rectangles **4** and **5**

Standard finite element codes apply multi-physics elements by which coupled thermal/mechanical or thermal/electrical

simulations can successively be realised. Such multi-physics elements are not available for the coupled heat transfer/superconductor stability problem. The "architecture" of the master scheme thus has to compensate the missing multi-physics elements.

At the end of step (5), the whole procedure, steps (1) to (5), is repeated as an iteration process until convergence is obtained to yield, in each of the load steps or sub-steps, a quasi-stationary (quasi-equilibrium) local temperature and transport current distribution. This result decides whether the superconductor is still in the zero-loss, current transport state or has reached a flux flow or an Ohmic resistance state.

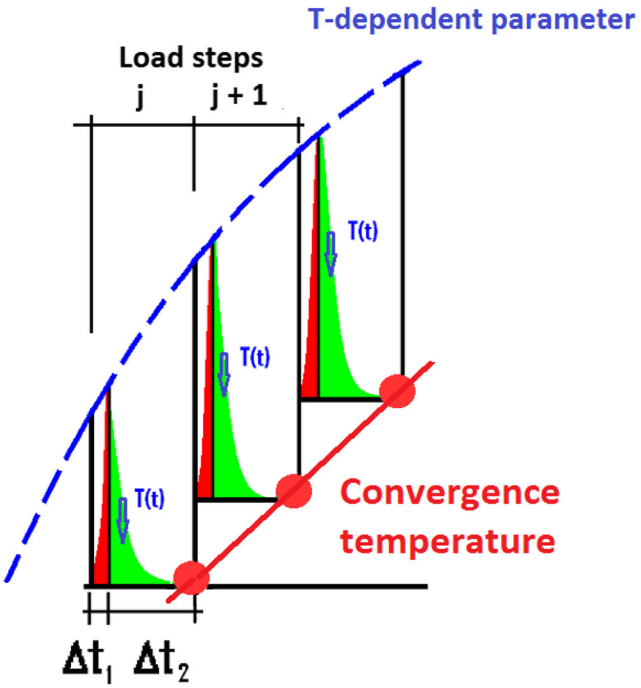

Fig. 13 Solution scheme used in the numerical simulations including a finite element (FE) procedure that is integrated in a master scheme (schematic, not to scale; compare text). The figure explains the tooth-like behaviour of nodal or element temperature. For incident radiation pulses, a Monte Carlo simulation is performed in the interval Δt_1, solution of Fourier's differential equation proceeds in the interval Δt_2; we have $\Delta t_1 << \Delta t_1$. For a single pulse, only one load step applies. For AC disturbances like a fault current, the full simulated period consists of a large number of full 2π-oscillation periods. Each period (duration 20 ms) is, for example, divided into 40 single load steps (each with $\Delta t_1 + \Delta t_2 = 5\ 10^{-4}$ s). Surface sources (at the target) and volume sources (both conductive and radiative) in a filament or in another conductor geometry are defined as start conditions, within each load step. The dashed blue curve indicates any parameter like specific resistance or heat, or thermal conductivity and also results of the calculations (like J_{Crit} or the stability function) that depends on temperature, $T(t)$, and that in turn drives the solutions for the temperature field $T(x,y,t)$. Convergence temperature is indicated by the large, solid red circles, at the end of each of the load steps, j. The FE program, by appropriately set convergence conditions, decides to which extent an initial differential integration time step, $\delta t \geq 10^{-14}$ s within the $\Delta t_{1,2}$ can be increased up to $\delta t \leq 10^{-5}$ s if length of the load step is $5\ 10^{-4}$ s, as presently. When the system thermally arrives at its convergence temperature, redistribution of transport current and of all electrical variables is assumed to occur quasi-instantaneously, with time constants small in relation to thermal relaxation time

All these calculations are performed with a large number N_{El} of finite elements (between 4000 and 30000). Internal standard FE convergence criteria in step (1) contribute to obtain stable quasi-equilibrium solutions of the Fourier problem, while in the peripheral components of the master scheme, it has to be controlled whether the output provides stable solutions for critical current density, magnetic field, values of resistance, fault states, electrical losses of the conductor (in total for all electrical and magnetic parameters relevant for current transport), for the Meissner states and for current distribution.

The flow chart in Fig. 12 explains operation of the master scheme.

As result of step (1), Fig. 13 schematically explains the saw-toothed behaviour of the solutions obtained for transient, local conductor temperature. The dashed blue curve indicates the variation of any of the input parameters (like thermal conductivity, specific heat of the conductor or critical current density). As an initial thermal excitation, we apply absorption of a radiative pulse, as a single point-like event, or a sudden increase of transport current to a fault; in this case, the disturbance is not point-like but in principle may extend to all grains or filaments or to the total cross section of a conductor cable.

Both events (an incident radiation pulse or a fault current) would be recognised at single localised or extended positions in the conductor cross section. Local temperature will increase in an interval Δt_1 in Fig. 13, as calculated in the FE part (step 1). The temperature increase changes the value of all temperature-dependent, local parameters like thermal diffusivity or critical current density and thus also of local resistances since transport current density might exceed critical current density and generate flux flow resistance.

The resistances are used as input for calculation of transport current distributions from the complete resistance network; the network is composed of the resistance of all (4000 to 30000) elements. Since the number of non-zero resistances might not be constant, and their values fluctuate (since they depend on local temperature), the transport current distribution, too, cannot be uniform. Transport current distribution may oscillate (percolate) through the cross section (compare e.g. [5, 6]).

This procedure, performed in each load step j, is with the present status of the master scheme repeated up to $N_{It} = 10$ times (the number N_{It} denotes iterative sub-steps). Note that the division of each load step j into N_{It} iterations is not identical to the (large) number M_j of standard, equilibrium FE iterations in each of the load steps and in each of the N_{It} sub-steps. The number M_j is set by the user or by the program itself, as standard parameters to obtain convergence in the FE solution procedure of Fourier's differential equation. The number N_{It} must be set by the user, from observation of the convergence behaviour of the system to the large circles in Fig. 13.

In case of absorption of a radiation pulse, first, a Monte Carlo simulation is performed in the interval Δt_1 in Fig. 13. The Monte Carlo simulation serves for definition of an initial distribution of radiative volume sources that is needed for the finite element analysis of the thermal conduction plus radiation problem. According to Carslaw and Jaeger [14], an initial temperature distribution is equivalent to a distribution of instantaneous, initial heat sources (like radiative). Conversely, once radiative sources are determined, here from the Monte Carlo calculations, this distribution in each load step is equivalent to an initial temperature distribution within the sample. The Monte Carlo simulation thus provides solutions of the equation of radiative transfer (see part A of this paper) in that it calculates all absorption/remission and scattering events. We in this case have surface sources (at the target) and volume sources (both radiative and conductive) within grains and filaments.

In case of absorption of a radiation pulse, with application of the Monte Carlo simulation and the solution of Fourier's differential (FDE) equation, temperature in the interval Δt_1 in Fig. 14 (see below) increases quickly; compare the red curve. The solution of the FDE continues in the interval Δt_2 to yield, after the end of the disturbance, the exponential decay of the temperature (indicated by green curves and dark-blue arrows). Since only one pulse is considered in this example, and because the absorption/remission and scattering events proceed very fast, we have $\Delta t_1 < < \Delta t_2$. In case there are repeated, oscillating pulses (Fig. 14), each pulse constitutes its own load step, with again $\Delta t_1 < < \Delta t_2$.

But in case of AC disturbances, like a fault current, the full simulated period may be extended to up to 10 full 2π-oscillation periods. Each period (duration 20 ms) is divided into 40 single load steps ($\Delta t = \Delta t_1 + \Delta t_2 = 5 \times 10^{-4}$ s) and each load step again divided by up to 10 sub-steps with equilibrium integrations.

Temperature evolution in both cases is calculated until it arrives at its convergence temperature in the load step j (large red circles in Fig. 13). In case the disturbance is given by a fault current, the red and green curves and the convergence temperatures (the large red circles) are repeated in each load step. This produces the saw-toothed scheme of the temperature development shown in this figure.

Transport current within the individual load steps of length $\Delta t = 5\ 10^{-4}$ s is constant but increases from load step j to the step j + 1 when simulating a fault. As mentioned, the transport current shall within a short period (here 2.5 ms) increase to a fault current with a large multiple of the nominal value (in the present calculations by a factor of 20).

By appropriate FE (i.e. internal) convergence conditions set for temperature evolution and heat flow, the FE program in step (1) decides to which extent an initial differential integration time step $\delta t \geq 10^{-14}$ s within the $\Delta t_{1,2}$ can be increased up to a maximum $\delta t \leq 10^{-5}$ s.

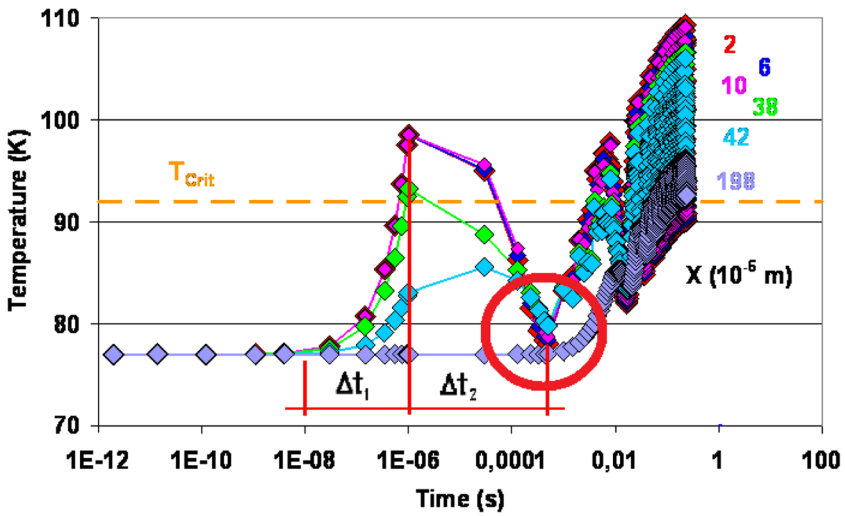

Fig. 14 Convergence of local element temperature (example) obtained in the simulation procedure (master scheme), as explained in Appendix 1 and in Fig. 13 with integrated intermediate finite element calculation steps. The figure shows element temperature excursion with time after an isolated but periodic thermal excitation by heat pulses on a YBaCuO 123 filament of 200 μm radius ($T_{Crit} = 92$ K, at zero magnetic field) before application of standard Powder in Tube manufacturing steps (material properties of the sample thus are close to those of the solid superconductor). Results refer to positions X from the centre of the circular filament. Time intervals Δt_1 (temperature increase due to absorption of the pulses) and Δt_2 (decrease of temperature because of conductive and radiative heat dissipation) are explained in the text. Convergence behaviour of the temperature resembles the saw tooth-like behaviour schematically indicated in Fig. 13. The large red circle indicates convergence temperature after a number N_{It} (a...k) of iterations (compare Fig. 12) within the load steps, j (the load steps in this diagram are identified by the computation time). At time $t > 0.01$ s, the saw tooth-like convergence behaviour can no longer be resolved, because of the logarithmic plot. The figure is taken from [7]

For an illustration of achieved convergence, compare solid diamonds, in particular the purple, red and blue symbols, between $10^{-8} \le t \le 10^{-4}$ s in Fig. 14 calculated for single isolated but periodically repeated disturbances (here, the repeated absorption of a single radiative pulse incident onto a small, point-like target positioned on a YBaCuO 123 filament).

While integration time steps, δt, are small, the length of the intervals Δt is large in comparison to characteristic (diffusion) time, τ_C, of electrical or magnetic fields and of currents, and of time τ_R needed to establish new quasi-equilibrium, electron charge distributions.

The solution scheme of the (proper) finite element problem (step 1) applied sparse matrix direct solvers which request large memory space. Alternatives (JCG or ICG iterative solvers) were tested but convergence is not guaranteed. In the present case, 4-node, plane model elements have been applied that allow rotation against axis of symmetry.

Stable operation of the conductor in an electrical grid can be disrupted by suddenly upcoming electrical resistances and corresponding losses that immediately transform into thermal energy. From the large spectrum of possible disturbances, only flux flow and Ohmic resistance losses have been considered in this paper.

Appendix 2: The Conductor.

The Powder in Tube manufacturing process comprises standard mechanical processes interleaved with repeated thermal treatment of the superconductor material. Rolling or hammering and other metallurgical methods align the grains horizontally (Fig. 1a-c in part A).

The better the alignment (the crystallographic ab-plains parallel to the horizontal grain axis), the better the current transport properties (in particular the critical current density) of grains and, consequently, of filaments, tapes and cables in these planes. Uniform horizontal orientation of all grains strongly improves also thermal transport in the same plane. But in vertical, c-axis direction, current and thermal transport are strongly limited because of a large number of electrical resistances (quasi Josephson junctions in the BSCCO 2223 crystals) and of interfacial electrical (weak links) and thermal resistances (very thin, insulating layers) between neighbouring grains and between grains and the Ag-matrix.

Thickness of the tape shown in Fig. 1b in part A is about 250 to 300 μm, with about 3 to 4 mm width and with strongly different geometrical dimensions of its embedded filaments and Ag-matrix inter-layers. Also, the solid thermal conductivity of the BSCCO 2223 material is strongly different from the conductivity of the Ag-matrix and is highly anisotropic. The same applies to electrical transport. Each filament (the black rectangles in the cross section), by surface roughness and weak links (to some extent closed, quasi surface inter-layers), is electrically and thermally decoupled from its neighbours and from the Ag-matrix material.

Onset of the Meissner effect within each filament may be quite different from the same effect in neighbouring filaments and even in neighbouring elements, as it depends on the local magnetic field and thus on local temperature distribution. The Meissner effects therefore have to be calculated in each of the up to 30000 elements.

Appendix 3. A model for calculation of the flux flow resistivity.

General aspects

The following is a summary that describes simulation of flux flow resistance. The model is suitable for calculation of flux flow losses by numerical procedures like the method of finite elements. This model was explained in detail in [12]. In this Appendix, we restrict its description to the physics behind, and the numerical modelling steps will not be repeated here. The readers interested in the numerical steps are invited to consult [12].

In Eq. (2), the resistivity ρ_{NC} usually is considered the room temperature (constant) normal conduction value of the superconductor solid material. However, this simple equation (i) is valid for only *homogeneous superconductor solids*, (ii) it is not at all clear that ρ_{NC} should be kept independent of temperature in calculations of flux flow resistivity. (iii) As was mentioned in [12], with corresponding citations to original literature, there may be deviations from Eq. (2) in type II superconductors, like YBaCuO or BSCCO, with large values of the Ginzburg-Landau parameter. (iv) Equation (2) without modifications does not appear to appropriately include any weak links between solid constituents (grains, domains) in microporous conductors as they might contain a variety of different structure (1D to 3D geometry) and material composition that each contribute to electrical resistance. (v) Direct experimental determination of ρ_{FF} is difficult, not only because flux creep, a competition to flux flow, operates in the background and can have different origins; flux creep inevitably rises with increasing temperature. (vi) While the idea to extract flux flow resistivity from the slope of the I/V or J/E-curves, pinning of vortices in high temperature superconductors (HTSC, because of their large anisotropy of current transport and of field penetration) neither can be limited to an atomistic structural view (like dislocations) nor do pinned vortices in HTSC reflect the comparatively simple geometrical structures (flux lines, vortices) found in low-temperature (metallic) superconductors.

Modelling Weak Links

Resistances, on the one hand, and on *nanoscopic* scale, exist as electrically insulating, quasi-interlayers between neighbouring crystallographic ab-planes, which means they can be interpreted

as natural quasi-Josephson junctions. Or the resistances as "weak links" appear, on *microscopic* dimensions, as 3D material "bridges" between neighbouring grains and domains (in high-temperature superconductors of good quality, as clusters of orthorhombic, parallel-oriented grains). There are also weak links consisting of 2D interfacial or 1D point contacts only.

In general, two paths are open to current transport through a particle bed like the agglomerate of grains shown in Fig. 1c of part A: The filament is composed of superconductor particles and of empty or filled voids. The voids might partly be filled with Ag-matrix or with weak link material (like different phases of superconductor material), *or* the voids result from pores that in turn result from materials or manufacture imperfections and are simply filled with air. Currents paths then are described as (a) intra-granular currents that in the Meissner state, as zero loss displacement and screening currents, yield zero internal magnetic field in individual particles and (b) inter-grain currents flowing through 3D, 2D and 1D contacts between neighbouring particles and multiples thereof; these currents not necessarily would be zero loss currents. Inter-grain paths open to current transport are of practical importance.

Either path can be assigned a corresponding resistivity. A total, effective resistivity, ρ_{eff}, then integrates all resistances opposed to intra- and inter-grain currents within an appropriately designed geometrical cell. We will use in Eq. (2), and thus in the finite element simulations, the effective resistivity, $\rho_{eff} = \rho_{eff}(\rho_{NC},T,B,g)$, as a function of temperature, magnetic field, B, and of geometry, g, instead of the traditional assumption ρ_{NC} constant. Equation (2) thus is written as $\rho_{FF} = \rho_{eff}B/B_{Crit2}$.

The direct dependence of ρ_{FF} on magnetic field, given by the factor B/B_{Crit2}, is taken into account solely in the finite element procedure. The indirect temperature dependency of ρ_{FF} results from $\rho_{eff}(\rho_{NC},T,B,g)$, which means from the temperature dependencies of all material parameters and fields entering the flux flow model, $\rho_{eff} = \rho_{eff}[\rho_{NC}(T),T(B),B(T),g]$ (apparently, this dependency is often neglected). An indirect temperature dependency of B and thus of ρ_{eff} results also from J_{Crit}, since screening current flow as critical currents and determine the magnitude of a partly penetrating external field. In view of these physical interdependencies, it is rather questionable whether the assumption of a constant (independent of temperature) flux flow resistivity, ρ_{FF}, can be justified.

More generally, even the structure of Eq. (2) seems to be questionable. An improved theory, still to be developed, might give up standard assumptions like a viscosity opposed to flow of

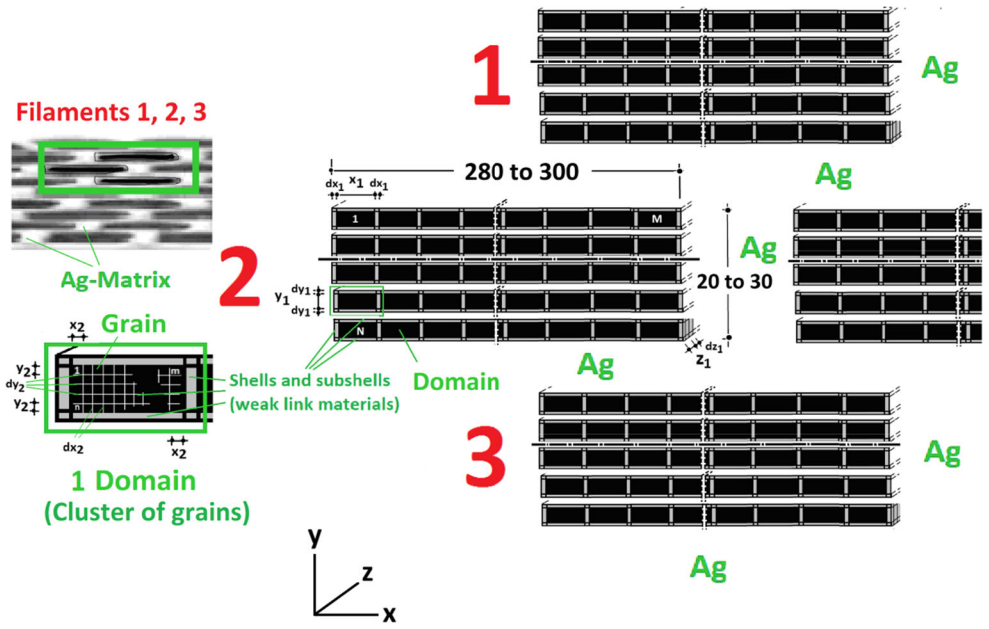

Fig. 15 Geometrical cell model for calculation of the resistivity, ρ_{NC}, and its effective value, ρ_{eff}, under normal conduction, to be applied in Eq. (2) for ρ_{FF} and thus in the finite element simulations. Above, left, the figure shows three arbitrarily selected filaments 1, 2 and 3 (schematic, no to scale; this is a detail of the tape cross section). Filaments (black, flat ellipses copied from the original figure, the Long Island Cable conductor) are approximated by black rectangles. Each filament (first detail, right) consists of a number $M \times N$ domains (clusters of orthorhombic plate-like, parallel oriented grains; schematic) each of which incorporate a superconductor core (the proper grain, large black rectangle) and a shell of weak link material (light-grey). Each of the $M \times N$ domains is divided into a number $N = m \times n$ grains (second detail, bottom part of the figure, left; schematic). This hierarchy of large and small superconductor cores in domains and grains and of correspondingly thick and thin shells and sub-shells facilitates modelling resistances of grains and weak link materials of different size, thickness, material composition, physical properties and field dependence, respectively. Total simulated conductor length, z, taken over large numbers of grains and domains is arbitrary. Numerical values indicating size of cross section of one filament in this figure are in micrometre. Resistances to current flow in z-direction of all domains and grains, filaments and Ag-matrix material are switched in parallel. The figure (with slight modifications) is taken from [12]

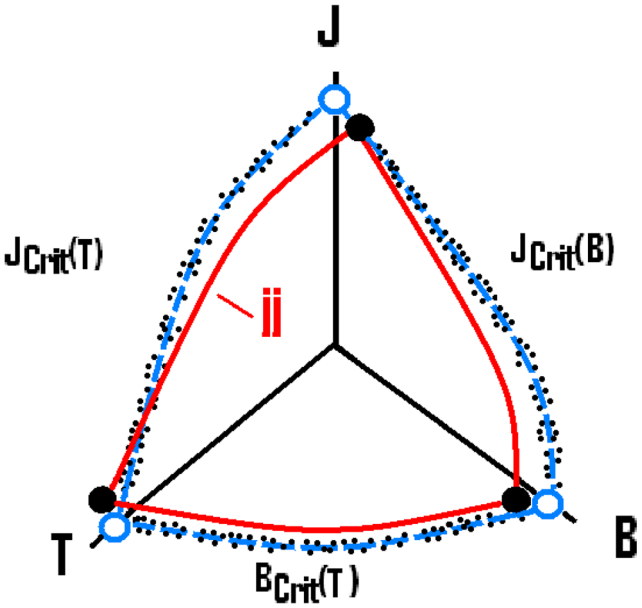

Fig. 16 Existence diagram of superconductivity (schematic, not to scale; the lower critical magnetic field is not shown), with random variations (small black dots) of $T_{Crit}(B)$, $J_{Crit}(B)$ and $J_{Crit}(T)$ against their conventional values; the variations are different in each of the superconductor elements. The thick black solid circles and the random distributions $T_{Crit}(B)$, $J_{Crit}(B)$ and $J_{Crit}(T)$ (red curves, shown for only one single element, *jj*, may significantly be shifted against the conventional critical values (open blue circles and dashed blue curves). The figure is taken from [9]

flux quanta in particle beds and therefore would suspend Eq. (2), except for application to homogeneous solids.

A provisional and practical way is to presently calculate ρ_{FF} by means of Eq. (2) in a network composed of superconductor grains and domains and weak links in-between, with the "effective" value ρ_{eff} of ρ_{NC}.

It is assumed in the following that the domains in Fig. 15 are built by staples of a large number of plate-like single grains that during sample preparation in powder in tube processes are pressed to a roughly ordered particle "bed", with the crystallographic ab-planes parallel to current flow, in Fig. 15 parallel to the x,z-plane.

A corresponding model reported by [15] describes total current of a 2223 tape conductor through a network of parallel weak and "strong" links, with strong field dependence of critical current density, J_{Crit}, in weak links but with dependence of J_{Crit} on flux pinning in strong links. Weak links in this model are regarded as Josephson junctions, and strong links are represented by the solid grain material. While separation with respect to field dependence of J_{Crit} principally appears to be sound, we believe the assumption of parallel (which, strictly speaking means, contactless) paths, like the imagination of separate "chains" (two individual current paths) would be too much an approximation to be successful. On the micro- and nanoscopic size level, grains and their weak links in reality are disorderly arranged; geometrically ordered structures become obvious not before grains are compressed to domains and to filaments, under thermomechanical treatment during Powder in Tube manufacture.

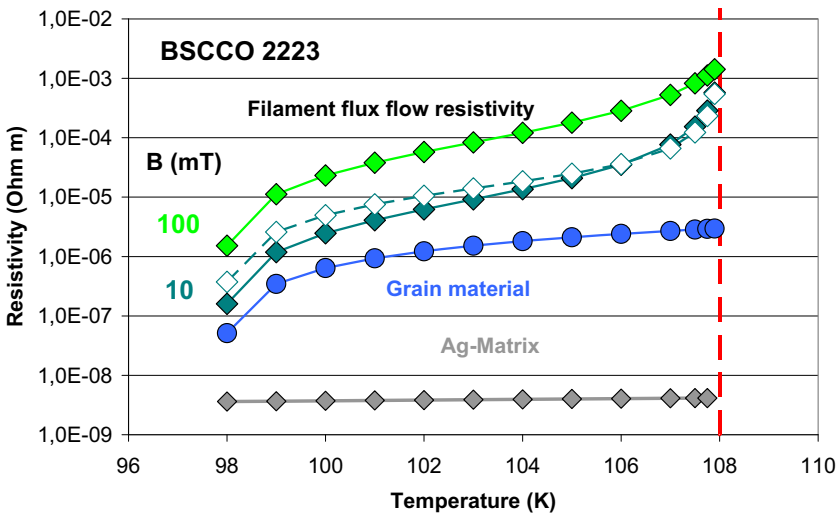

Fig. 17 Flux flow resistivity, ρ_{FF}, calculated from the effective ρ_{eff}(compare text) and with the field factor $B/B_{Crit,2}$ in Eq. (2) to current transport of a multi-filamentary BSCCO 2223 conductor, for local (constant) magnetic flux density, $B = 10$ and 100 mT (solid dark-green and light-green diamonds, respectively). Calculation of the resistivity follows Fig. 15. Dimensions of domains, x_1, y_1 and z_1, are 70, 6 and 70 μm and thicknesses dx_1, dy_1 and dz_1 of weak link shells enclosing domains are 100, 10 and 100 nm, respectively. Dimensions of grains x_2, y_2 and z_2 are 20, 1 and 20 μm and thicknesses dx_2, dy_2 and dz_2 of weak link shells surrounding grains are 1, 1 and 1 nm, respectively. Solid blue circles indicate ρ_{Grain} as solely the grain core (bulk) material without magnetic field and under zero current (note the temperature range is reduced to $96 \le T \le 108$ K). Open dark-green diamonds denote conventional ρ_{FF} from [20] calculated with B = 10 mT. For comparison, dark-grey diamonds indicate resistivity of the Ag-matrix material. The upper critical magnetic field, at $T = 4.2$ K, is $B_{Crit,20} = 200$ T giving $B_{Crit,2}(T) = B_{Crit,20}\,[1 - (T/T_{Crit})^2]$. Critical temperature (vertical, dashed red line, for $B = 0$ and very small current) is 108 K. The figure is taken from [12]

Flux Flow Resistance Obtained from a Cell Model

In the cell model approximation (Fig. 15), we in the first step extract the resistivity of the proper (ideal, *zero porosity*) solid (bulk) material from measurements of the resistivity of a multi-filamentary, *polycrystallin*e Powder in Tube (PIT) conductor. The PIT conductor for its modelling is not ideally suited at all, but this lack, to obtain the zero porosity value, shall be compensated by application of an appropriate model describing conduction in particle beds. The model must allow extraction of the (zero porosity) resistivity of the *solid* material from the total resistivity of a *particle bed* (what we obtain in this way is, to some extent, a virtual value that of course depends on the assumed model).

Applying instead the resistivity of *bulk* (solid, pure) material in the simulations is not recommended for this step: The bulk material does not undergo the special mechanical and thermal treatments usually applied during manufacture of PIT-conductors. The resistivity of proper, pure bulk material samples (and other properties) thus will be strongly different from the resistivity of the solid part of samples when they finally leave the PIT process (the process implies a variety of mechanical and thermal manufacturing steps).

The uncertainty inherent in this way to extract the zero porosity value of the solid part of the particle bed is considered as smaller than the uncertainty that would result from application of the solid resistivity of (pure) bulk material in the numerical simulations. But to be successful, the model to extract the zero porosity value must be well established, with experimental evidence.

This extraction will be made from the resistivity of BSCCO 2223; resistivity of this material is accessible from the literature. After the first step, and now again with the same cell model, the extracted (virtual, zero porosity resistivity) is converted to the resistivity of weak link material, resident on the periphery of grains and domains.

A "historical" cell model, the Russell cell model [16], shall be applied for these steps. It is easy to handle since it just contains porosity and the resistivity of both (solid and porous) phases, either for electrical or thermal transport. It is flexible (the role of particles and voids without much effort can be interchanged); the results roughly are independent of size of the constituents, and though the model in its original scope applies to a regular distribution of cubic particles, it is according to experience applicable to particulates of also other shape and of modestly irregular spatial distribution. In the present case, for application of Russell's cell model, the "particulates" are grains and domains distributed in a filament, with tiny voids of nanoscopic dimensions in-between that house weak links. Provided their geometry and material composition can adequately be indicated, there is no reason to believe the model could fail severely.

Small porosity in this picture indicates that weak links occupy only a small volume fraction in relation to the volume of the superconductor solid phases (grains, domains).

The Russell cell model does not assume particles or voids arranged in coherently connected, non-interacting chains. Instead, particles and voids are interpreted as distributed obstacles to current flow. The cell model treats all resistances that contribute to the (spatial) average ρ_{eff} *as if* they would be randomly distributed.

The conductor cross section (Fig. 2a,b of part A) thus shall be mapped upon a geometrical cell model (Fig. 15, schematic) that allows application of the Russell cell model. The geometrical structure assigns each of its particular solid cross sections (grains, domains, filaments and voids partly filled with weak link material) a specific resistivity. These have to be calculated, from repeated application of the Russell cell model, in a series of successive approximations (for this purpose, all these have to be assigned a specific porosity).

Repeated Application of Russell's Cell Model

Division of the 91 filaments in the multi-filamentary conductor (black rectangles in Fig.15, schematic) into M × N domains, and each domain into m × n grains, results in a three-level hierarchy ("large" domains, "small" grains, "tiny" weak links). Each domain is composed of a solid core (the proper superconductor, black rectangles) and of "shells" (light-grey sections) that indicate weak link materials arranged around the black cores. Each grain incorporates its own superconductor core (again black rectangles) and corresponding sub-shells (thin white lines, now the weak links between the grains). Electrical and thermal transport through the Ag-matrix material, of well-known resistivity, is accounted for solely in the finite element scheme.

Micro- or nanoscopic metallurgical sections or SEM pictures are not available, the resolution of which would allow more than just getting very rough impressions of spatial structure and porosity of 3D weak link materials. Also, the tiny dimensions of weak links cannot be concluded from experiments. Weak links in addition might even consist of only 2D interfacial or 1D point-like contacts.

In a qualitative view, porosity Π_{Shell} of weak link materials between domains probably is much larger than the corresponding Π_{Shell} of weak links between grains, and porosity will increase with radial distance from position of inner-lying grains. This is because manufacture of PIT superconductors is subject to robust thermomechanical treatments; the conductors experience large frictional (from thermal expansion, winding) and compressive forces, the latter due to mechanical shock treatment (forging, down-hammering, rolling). Since the superconductor material is very hard, the very first "receiver" of compressive and frictional load is the domain periphery, so that

particle surfaces at these positions, in very thin surface layers, may be ground to almost a powder, in contrast to grains located (and thus mechanically protected) in the deep interior. Weak links between grains thus would contribute stronger to mechanical stability of the bed, in parallel to the matrix jacket, than weak links between domains. Assigning large Π_{Shell} (close to 1) to *domain* weak links simultaneously assumes that the corresponding weak links are *poor* superconductor phases distributed in the proper BSCCO 2223 material.

Values of the porosity Π_{Shell} of weak links between *grains* again can be estimated only but this material would be *rich* in superconductor phase. Whether in a melt the periphery of grains and domains is sharply defined depends on surface tension and decay rate of temperature, but we can expect that concentration of the proper superconductor material does not sharply break down to almost zero at the periphery; a finite concentration gradient is more probable.

But other BSCCO superconductor phases and probably existing contaminations may contribute to the resistivity of weak links, in different ways, however. This has been accounted for in this model by separation of weak link resistivity according to magnetic field dependence: The resistivity is split into the proper field-dependent BSCCO phase (which means, below its $T < T_{Crit} = 108$ K) and in the other BSCCO phases that do not (or do no longer, at elevated temperature) depend on magnetic field, and thus cannot contribute to ρ_{FF}. Normal conducting "foreign" contributions (contaminations) to the resistivity of weak links have to be eliminated from ρ_{FF}, too.

Thermal Analogue to Weak Links

After (a partly reverse) application of Russell's cell model to estimate *material* properties of grain, domain and shell cross sections, the *geometrical* aspect of calculating the effective resistivity of the cell remains to be solved: Shell cross sections have to be reduced to point-like contacts, in order to describe weak links.

No experimental values are available on size or on number of electrical contacts and on their distribution on superconductor particle surfaces and interfaces. Modelling of electrical resistance in normal particle beds originally goes back to Rayleigh and Maxwell and has been revisited by Holm [17]. Kaganer [18] and several authors cited in this reference have converted the results from electrical transport to the analogous thermal transport problem. In turn, refinements achieved in heat flow-related studies can be used for solution of the present electrical transport problem in a two-phase medium (grains or domains and weak links).

To solve this problem, a resistance cell unit between two spheres, with partial thermal or electrical resistances, is described in [12] (and goes back to [18]) again with citations to original literature including constriction zones, Hertz' contact theory and radii, but will not be repeated here. Please consult this reference and the original literature.

References

1. Wilson, M.N.: Superconducting magnets. In: Scurlock, R.G. (ed.) Monographs on Cryogenics. Oxford University Press, New York, reprinted paperback (1989)
2. Dresner, L.: Stability of superconductors. In: Wolf, St. (ed.) Selected Topics in Superconductivity. Plenum Press, New York (1995)
3. Flik, M.L., Tien, C.L.: Intrinsic thermal stability of anisotropic thin-film superconductors. ASME Winter Ann. Meeting, Chikago (1988)
4. Reiss, H.: Superconductor stability against quench and its correlation with current propagation and limiting. J. Supercond. Nov. Magn. **28**, 2979–2999 (2015)
5. Reiss, H.: Inhomogeneous temperature fields, current distribution, stability and heat transfer in superconductor 1G multifilaments. J. Supercond. Nov. Magn. **29**, 1449–1465 (2016)
6. Reiss, H.: Radiative transfer, non-transparency, stability against quench in superconductors and their correlations. J. Supercond. Nov. Magn. (2018). https://doi.org/10.1007/s10948-018-4833-2
7. Reiss, H., Troitsky, O. Yu. Superconductor stability revisited: impacts from coupled conductive and thermal radiative transfer in the solid. J. Supercond. Nov. Magn. **27**, 717–734 (2014)
8. Marzahn, E.: Supraleitende Kabelsysteme, Lecture (in German) Given at the 2nd Braunschweiger Supraleiter Seminar, Technical University of *Braunschweig - elenia,* Germany, (2007)
9. Reiss, H.: Stability considerations using a microscopic stability model applied to a 2G thin film coated superconductor. J. Supercond. Nov. Magn. **31**, 959 (2017). https://doi.org/10.1007/s10948-017-4245-8
10. Huebener R. P., Magnetic flux structures in superconductors, Springer Series in Solid-State Sciences **6**, Springer-Verlag, Berlin, Section 7.3. (1979)
11. Tilley D. R., Tilley J., Superfluidity and superconductivity, 2nd Ed., Graduate Student Series in Physics, Adam Hilger Ltd, Bristol and Boston (1986), Section 6.5.2
12. Reiss, H.: Finite element simulation of temperature and current distribution in a superconductor, and a cell model for flux flow resistivity – interim results. J. Supercond. Nov. Magn. **29**, 1405–1422 (2016)
13. Reiss, H.: A microscopic model of superconductor stability. J. Supercond. Nov. Magn. **26**(3), 593–617 (2013)
14. Carslaw H. S., Jaeger J C, Conduction of heat in solids, 2nd Ed., Oxford Science Publ., Clarendon Press, Oxford (1959), reprinted (1988) 356
15. Van der Laan, D.C., van Eck, H.J.N., Ten Haken, B., Schwartz, J., ten Kate, H.H.J.: Temperature and magnetic field dependence of the critical current of $Bi_2Sr_2Ca_2Cu_3O_x$ tape conductors. IEEE Transacts. Appl. Supercond. **11**(1), 3345–3348 (2001)
16. Russell, H.W.: Principles of heat flow in porous insulators. J. Am. Ceram. Soc. **18**, 1–5 (1935)
17. Holm, R.: Electric Contacts. Springer Verlag, Berlin, Heidelberg (1967)
18. Kaganer M. G., Thermal Insulation in Cryogenic Engineering, Israel Progr. Sci. Transl, Jerusalem (1969)
19. Phelan, P.E., Flik, M.I., Tien, C.L.: Radiative properties of superconducting Y-Ba-Cu-O thin films. Journal of Heat Transfer, Transacts. ASME. **113**, 487–493 (1991)
20. Shimizu, H., Yokomizu, Y., Goto, M., Matsumuara, T., Murayama, N.: A study on required volume of superconducting element for

flux flow resistance type fault current limiter. IEEE Transacts. Appl. Supercond. **13**, 2052–2055 (2003)
21. Vojta M., Quantum phase transitions, arXiv:cond-mat/0309604v2 (2003)
22. Greiner, M., Mandel, O., Esslinger, T., Hänsch Th, W., Bloch, I.: Quantum phase transition from a superfluid to a Mott insulator in a gas of ultracold atoms. Nature. **415**, 39–44 (2002)
23. Poole Jr., C.H.P., Datta, T., Farach, H.A.: Copper oxide superconductors. John Wiley & Sons, New York (1988)
24. Suzuki M, Suzuki I S, Lecture notes on solid state physics, AC magnetic susceptibility, State University of New York at Binghamton (2009)